

Impact of Electric Current Fluctuations Arising from Power Supplies on Charged-Particle Beams: A Measurement-Based Stochastic Noise Model of Fermilab's Booster Synchrotron

Phil S. Yoon*

¹ *Department of Physics and Astronomy, University of Rochester, Rochester, NY 14620, U.S.A.*

(Dated: January 24, 2008)

Electric current fluctuations are one type of unavoidable machine imperfections, and induce magnetic-field perturbations as a source of instabilities in accelerators. This paper presents measurement-based methodology of modeling the fluctuating electric current arising from the power system of Fermilab's Booster synchrotron to discuss the ramifications of the presence of ripple current and space-charge defocusing effects. We also present the method of generating stochastic noise and the measurement and analysis methods of ripple current and offending electromagnetic interferences residing in the Booster power system. This stochastic noise model, accompanied by a suite of beam diagnostic calculations, manifests that the fluctuating power-supply current, when coupled to space charge and impinging upon a beam, can substantially enhance beam degradation phenomena—such as emittance growth and halo formation—during the Booster injection period. With idealized and uniform charge-density distribution, fractional growth of rms emittances due to ripple current under space charge turn out to be about 8 ~ 9 % in both transverse planes over the injection period of 2.2 ms prior to beam acceleration.

PACS numbers: 05.40.-a, 07.05.Tp, 43.50.Yw, 43.60.Cg, 77.22.Jp, 84.30.Jc

Contents			
		C. Moments	14
		D. RMS Emittances	15
I. INTRODUCTION AND MOTIVATION	2	IX. IMPACT OF GMPS CURRENT	
II. MODELING METHODOLOGY	2	FLUCTUATIONS WITH SPACE CHARGE	16
III. CLASSIFICATIONS OF NOISE	3	A. Couplings	19
A. External Noise	3	B. Coupling Magnitude	20
B. Electromagnetic Interferences	3	C. Halo Amplitudes	21
IV. STOCHASTIC PROCESS	3	X. CONCLUDING REMARKS	22
A. Langevin Equation	3	Acknowledgments	22
B. Ornstein-Uhlenbeck Process	4	References	22
C. Markov Process	4		
V. NON-WHITE NOISE GENERATION	4		
A. Stochastic Properties	4		
B. Box-Muller-Like Transformation	5		
C. Application of Noise to Macroparticles	7		
VI. GRADIENT-MAGNET POWER-SUPPLY (GMPS) SYSTEM	7		
VII. NOISE-MEASUREMENT TECHNIQUES AND ANALYSIS	7		
A. Common-Mode Noise and Differential-Mode Noise	7		
B. Power Spectral Density of Noise: FFT Analysis	12		
C. Parameterization of GMPS Noise	12		
D. Equivalent-Circuit Model	13		
VIII. TRACKING AND BEAM DIAGNOSIS	13		
A. Simulation Parameters	13		
B. Parallelized Calculations	14		

*Electronic address: syoon@fnal.gov

I. INTRODUCTION AND MOTIVATION

As is common in other natural systems, fluctuations are observed in particle accelerator systems. An ensemble of charged particles is defined as a *system*, and all the beamline components (magnets, power supplies, RF cavities, beam position monitors, etc.) for accelerating and guiding particles as *environment*, or *surroundings*. The system of a charged-particle beam perceives the environment of beamline components as a source of noise as illustrated by FIG. 1. External

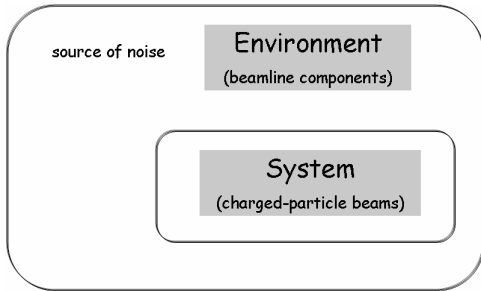


FIG. 1: System and surroundings

noise is intrinsic to particle accelerators of all types due to inevitable machine imperfections; e.g., ripple current from power supplies, ground vibration motion, etc. After being motivated by earlier findings from an idealized and simplified theoretical model [1], it was speculated that the adverse influence of power-supply current fluctuations possibly account for beam loss phenomena during the injection process of the Booster. Hence, an independent and novel approach has been made to build a *realistic* stochastic noise model, based upon a series of noise¹ measurements, to investigate and explore the impact of current fluctuations on charged-particle beams of the Booster at injection energy.

II. MODELING METHODOLOGY

For investigations of the impact of power-supply current fluctuations on charged-particle beams in an accelerator lattice structure, we began with building a preliminary noise model. As a first step, we designed and added a new physics module for generating stochastic noise to the existing ORBIT-FNAL package [2]. The new noise module is capable of generating a wide spectrum of stochastic noise employing the Ornstein-Uhlenbeck stochastic process [3] and a Langevin-like stochastic differential equation [4].

Prior to detailed experimental measurements, we corroborated with the preliminary noise model with a linear accelerator lattice that non-white, or colored noise could possibly en-

hance beam degradation process. These preliminary findings are consistent with earlier findings from an idealized and simplified model of collective space-charge modes coupled with dynamic noise [1].

As a next step, in addition to adding the new noise module to the ORBIT-FNAL, the existing *TeaPot* module was upgraded to establish Fermilab's Booster ring using a TEAPOT-style Booster lattice, and the *Diagnostic* module with new parallelized beam diagnostic calculations: *actions*, *halo amplitudes*, etc.

As confirmed with the preliminary model, we proceeded to devise methods for direct measurements of common-mode and differential-mode voltages, and ripple current in the electric current. Repeated measurements and Fourier analysis confirm that a substantial amount of noise, which can be transmitted to the magnet system, is indeed present in the power system. In addition, we performed equivalent-circuit simulation for potential offending resonances floating around the magnet system.

Based upon the measurement data and the results of Fourier analysis, parameterization of Booster ripple current is achieved by means of matching power spectral densities between measured ripple current and modeled Ornstein-Uhlenbeck (O-U) noise [3]. While translating modeled O-U noise to induced magnetic-field fluctuations, we tracked macroparticles in the presence of 3-D space-charge effects.

The following FIG. 2 and FIG. 3 illustrate the multi-stage approach to the stochastic noise modeling. For the purpose of the parameterization of ripple current to tune up the noise model, mapping from an experimental *signature space* to a stochastic *parameter space* was done. As a consequence, matching power spectral densities between physical noise and modeled O-U noise was achieved.

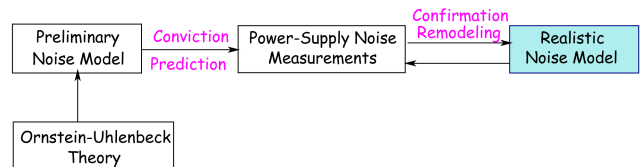


FIG. 2: Multi-stage approach to modeling the impact of power-supply noise on a beam

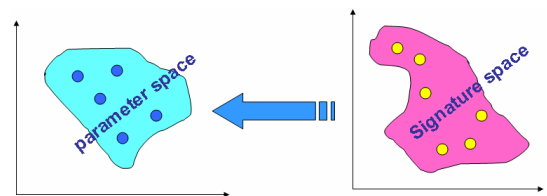


FIG. 3: Mapping from an experimental signature space to a stochastic parameter space

¹ In the present context, we will use the terms (*power-supply*) *noise* and *current fluctuations* and *ripple current* interchangeably.

III. CLASSIFICATIONS OF NOISE

In general, noise can be categorized into two types: *external noise* and *internal noise*. In our stochastic noise model, ripple current arising from Gradient Magnet Power Supplies (GMPS) of the Booster are regarded to be fluctuating external influences acting on charged-particle beams (see FIG. 1).

A. External Noise

External noise is originated from a source outside of the system; that is, beamline components. Since the effects of external noise can be described by a stochastic differential equation (SDE)², we choose Langevin Equation (LE) as SDE for indeterministic current fluctuations arising from each GMPS unit. It should be noted that power-supply ripple current is considered *indeterministic*, *random*, and *aperiodic*, in the sense that it never exactly repeats itself.

B. Electromagnetic Interferences

Electromagnetic-Interference (EMI) noise [6, 7] results from rapid changes in voltage and current in a power supply. Transmissions of EMI noise are characterized as either *radiative*, or *conductive*. Conductive EMI noise, such as differential-mode (DM) and common-mode (CM) noise, is usually several orders of magnitude higher than the radiative EMI, and can be more harmful to the system. Given impedance ($Z(\omega)$) as a function of frequency, fluctuations in common-mode voltage (V_{CM}) create common-mode current (I_{CM}), in addition to the inherent ripple current arising from sudden potential changes in the power-supply system. The EMI problem is thereby worsened and could result in larger current fluctuations, or common-mode current, or severe system damage.

IV. STOCHASTIC PROCESS

Of several different stochastic processes³, such as Liouville process, Poisson process, Wiener process, etc., we choose the Ornstein-Uhlenbeck process to represent electrical current fluctuations as classified in the preceding subsection.

A. Langevin Equation

In 1908, after the formulation of the Brownian movement by Einstein and Smoluchowski [8, 9], P. Langevin introduced the concept of the equation of motion of a stochastic variable (i.e., the position coordinate of a Brownian particle) [10]. Langevin Equation (LE) is considered to be the first example of a Stochastic Differential Equation (SDE)⁴. Langevin wrote the equation of motion for a Brownian particle according to Newton's second law under the assumption that a Brownian particle is subject to two forces: *damping force* (\mathcal{F}_d) and *fluctuating force* (\mathcal{F}_f)

$$\mathbb{F}(t) = \mathcal{F}_d(t) + \mathcal{F}_f(t) \quad (1)$$

$$m \frac{d^2\chi(t)}{dt^2} = \underbrace{-\zeta \frac{d\chi(t)}{dt}}_{\text{systematic force: dissipation}} + \underbrace{\mathcal{F}_f(t)}_{\text{stochastic force: fluctuation}} \quad (2)$$

Here, $\mathbb{F}(t)$, m , χ , and ζ represent the total force, particle mass, displacement, and the friction coefficient, respectively. The first term ($-\zeta \dot{\chi}(t)$ ⁵) on the right-hand side of Eqn. (2) represents the viscous drag as a function of time, or dynamic friction. The second term $\mathcal{F}_f(t)$ represents fluctuations which could be from white noise, or non-white noise⁶. The form of Eqn. (2) can be transformed to Eqn. (3) of first order. For modeling physical noise of the Booster power system, we employed *non-white* noise, or *off-white* noise in our investigations.

$$\dot{v}(t) + \alpha v(t) = \mathcal{L}(t), \quad (3)$$

where $\mathcal{L}(t)$ is a stochastic driving force, and α represents ζ/m . The following assumptions are made about the fluctuation part $\mathcal{L}(t)$:

- (1) $\mathcal{L}(t)$ is a function of time only, and independent of χ .
- (2) $\langle \mathcal{L}(t) \rangle = 0$
- (3) The variation rate of $\mathcal{L}(t)$ is much faster than the velocity of a Brownian particle, $v(t)$. Hence, the autocorrelation function $C_{\mathcal{L}}(t, t')$ is of Dirac- δ function; i.e.,

$$\langle \mathcal{L}(t) \mathcal{L}(t') \rangle = \mathcal{A} \delta(t - t') \quad (4)$$

The expressions above define the statistical properties of $\mathcal{L}(t)$. There is a great advantage in using LE instead of using Fokker-Planck Equation (FPE) of mathematical complex. The Langevin's method is much easier to understand than the FPE since it is based upon the time evolution of a stochastic variable, whereas the FPE applies to the time evolution of the

² A stochastic differential equation is a differential equation (DE) in which the coefficients are random functions of the independent variable, which is usually *time*.

³ In this paper, we use terms *stochastic process*, *stochastic function*, *random process*, *random function* and *process* interchangeably.

⁴ A stochastic differential equation is a differential equation with a stochastic (random) term. Therefore, its solution is also a random function.

⁵ The notations, $\dot{\chi}$ and $\ddot{\chi}$, denote $d\chi/dt$ and $d^2\chi/dt^2$, respectively.

⁶ *White noise* is noise with a flat frequency spectrum.

probability distribution. As such, LE allows us to dispense with the calculation of the diffusion coefficient, thus reducing associated mathematical complications. As a consequence, we built an effective but far more simplified model of stochastic noise.

B. Ornstein-Uhlenbeck Process

As in Eqn. (3), LE for Brownian motion is given as,

$$\dot{\xi}(t) + \omega\xi(t) = \mathcal{L}(t) \quad (5)$$

As explained in the preceding subsection, LE is associated with δ -correlated Gaussian stochastic forces of statistical properties. This stochastic process $\xi(t)$ is referred to as an O-U process. Note that the noise strength \mathcal{A} does not depend on the variables ξ . Since the O-U stochastic process is inherently to represent the velocity of a Brownian particle, it is the appropriate choice of stochastic process for modeling electric noise, or current fluctuations [3]; i.e., a time-derivative of electric charge (dQ/dt). Both position ($x(t)$) and velocity ($v(t)$) describe Langevin's Brownian motion. However, by utilizing the O-U process of the velocity of a Brownian particle, Langevin Equation can be reduced to a 1st-order linear stochastic differential equation that is derived from Newton's 2nd law. As a result, given initial conditions, LE as a 1st-order SDE is straightforward to find solutions.

The O-U process is associated with an exponentially-decreasing autocorrelation function $C_{\xi}(t, t')$ [11] and a finite autocorrelation time τ_{ac} [3]⁷.

$$C_{\xi}(t, t') = \langle \xi(t)\xi(t') \rangle = \mathcal{A}\exp(-\omega_{ac}|t - t'|), \quad (6)$$

where $\tau_{ac} = \omega_{ac}^{-1}$.

in which $\xi(t)$, ω_{ac} , and \mathcal{A} are a stochastic function, an autocorrelation frequency, and a constant noise strength, respectively. O-U processes are associated with the following probability density function:

$$\mathcal{W}_1(\xi, t) = \frac{1}{\sqrt{\pi\mathcal{A}/\omega_{ac}}} \cdot \exp\left(-\frac{1}{2} \frac{\xi^2}{\mathcal{A}/2\omega_{ac}}\right) \quad (7)$$

According to the Doob's theorem [12], the O-U process is the only stochastic process with all of the following properties: (1) stationary process, (2) Gaussian process, (3) Markovian process. In particular, if a process is invariant to translations in time (e.g. a shift in time (α)) then the process is called a *stationary process* [4, 13]. For a stationary process, we can make the following simplifications:

$$\langle \xi(t_1 + \alpha)\xi(t_2 + \alpha) \cdots \xi(t_n + \alpha) \rangle = \langle \xi(t_1)\xi(t_2) \cdots \xi(t_n) \rangle \quad (8)$$

where $\xi(t)$ is the stochastic function and $\langle \dots \rangle$ is the statistical average. The form of Eqn. (8) above implies the followings:

- (1) Since the underlying mechanisms causing the fluctuations do not change with time, the stochastic properties of a stationary process are conserved.
- (2) The important parameter in the O-U process is *relative time* and not the absolute time.

$$\langle \xi(t_1 - \alpha)\xi(t_1) \rangle = \langle \xi(t_1)\xi(t_1 + \alpha) \rangle \quad (9)$$

Therefore, the autocorrelation function $C_{\xi}(t, t')$ for a stationary process is a function of $|t - t'|$ only.

- (3) The ensemble average and the time average are the same, which leads to the ergodic property.

C. Markov Process

Markov processes involve the use of *conditional probability*.

$$\mathcal{W}_2(\xi_1, \xi_2, t) = \mathcal{W}_1(\xi_1)\mathcal{P}_2(\xi_1 | \xi_2, t) \quad (10)$$

The Markov process is therefore defined as follows [4]:

$$\mathcal{P}_n(\xi_1 t_1, \xi_2 t_2, \dots, \xi_{n-1} t_{n-1} | \xi_n t_n) = \mathcal{P}_2(\xi_{n-1} t_{n-1} | \xi_n t_n) \quad (11)$$

The form of Eqn. (11) implies that all the \mathcal{P}_n for $n > 2$ can be derived, when only \mathcal{P}_2 is known. In other words,

Only the present condition determines the future condition.

In order to avoid unnecessary mathematical complexity in building a stochastic noise model, we exploited the Markovian property. This is another reason why, of all the stochastic processes, the O-U process is a convenient choice for modeling the Booster ripple current.

V. NON-WHITE NOISE GENERATION

A. Stochastic Properties

LE governs an O-U process. Hence, if we use an O-U process to model GMPS current fluctuations, we need to solve LE. By solving the convenient 1st-order linear LE, we were able to extract more statistical properties of the O-U process in addition to Eqns. (4) and (7).

Let us first consider a 1st-order SDE of the form of LE.

$$\dot{\xi}(t) = f(\xi) + \eta(t) \quad (12)$$

Here $\eta(t)$ is non-white Gaussian noise with the autocorrelation function C_{η} :

$$C_{\eta}(t, t') = \langle \eta(t)\eta(t') \rangle = \frac{\mathcal{A}}{2\omega_{ac}} \exp(-\omega_{ac}|t - t'|) \quad (13)$$

⁷ The autocorrelation function $C(t, t')$ determines the property of a stochastic process of interest.

Non-white noise η is governed by LE with a white-noise driving force of $\mathcal{L}(t)$:

$$\dot{\eta}(t) + \omega_{ac}\eta(t) = \mathcal{L}(t) \quad (14)$$

The autocorrelation function $C_{\mathcal{L}}$ is δ -correlated with a strength \mathcal{A} :

$$C_{\mathcal{L}}(t, t') = \langle \mathcal{L}(t)\mathcal{L}(t') \rangle = \mathcal{A}\delta(t-t') \quad (15)$$

Ornstein and Uhlenbeck [3], Doob [12], and van Kampen [4] use the integration method to find the statistical properties of non-white noise, or colored noise from LE. We, on the other hand, solve LE as a 1st-order DE. The general solution of a 1st-order inhomogeneous DE is a linear superposition of a homogeneous solution (η_h) and a particular solution (η_p). Hence,

$$\begin{aligned} \eta(t) &= \eta_h(t) + \eta_p(t) \\ &= \eta(0) \cdot \exp(-\omega_{ac}t) + \int_0^t ds \cdot \exp(-\omega_{ac}(t-s)) \cdot \mathcal{L}(s) \end{aligned} \quad (16)$$

From Eqn. (16), the stochastic process at the next time step $t + \Delta t$ can be obtained.

$$\begin{aligned} \eta(t + \Delta t) &= \eta(0) \exp(-\omega_{ac}(t + \Delta t)) \\ &+ \int_0^{t + \Delta t} ds \exp(-\omega_{ac}(t + \Delta t - s)) \mathcal{L}(s) \\ &= \exp(-\omega_{ac}\Delta t) \eta(t) + \underbrace{\int_t^{t + \Delta t} ds \exp(-\omega_{ac}(t + \Delta t - s)) \mathcal{L}(s)}_{\mathcal{H}(t, t + \Delta t)} \end{aligned} \quad (17)$$

Let $\mathcal{H}(t, t + \Delta t)$ be the second term of Eqn. (17).

$$\mathcal{H}(t, t + \Delta t) \equiv \int_t^{t + \Delta t} ds \cdot \exp(-\omega_{ac}(t + \Delta t - s)) \cdot \mathcal{L}(s) \quad (18)$$

By transforming the variables of integration we can obtain

$$\begin{aligned} \mathcal{H}(0, \Delta t) &= \int_0^{\Delta t} d\tilde{s} \cdot \exp(-\omega_{ac}(\Delta t - \tilde{s})) \cdot \mathcal{L}(\tilde{s} + t) \\ &= \exp(-\omega_{ac}\Delta t) \cdot \int_0^{\Delta t} d\tilde{s} \cdot \exp(\omega_{ac}\tilde{s}) \cdot \mathcal{L}(\tilde{s} + t) \end{aligned} \quad (19)$$

By squaring Eqn. (19), we obtain

$$\begin{aligned} \mathcal{H}^2(0, \Delta t) &= \exp(-2\omega_{ac}\Delta t) \int_0^{\Delta t} \int_0^{\Delta t} d\tilde{s} d\tilde{s}' \exp(\omega_{ac}(\tilde{s} + \tilde{s}')) \mathcal{L}(\tilde{s} + t) \mathcal{L}(\tilde{s}' + t) \end{aligned} \quad (20)$$

The statistical properties of a random variable can be investigated by the calculations of various moments. We calcu-

late the first and the second central moments⁸ by averaging Eqns. (19) and (20) over an ensemble of particles. The first two moments determine the complete statistical properties of the O-U noise because it is a Gaussian process. Gaussian white noise has zero mean. For zero-mean Gaussian, the 1st moment vanishes.

$$\langle \mathcal{H}(0, \Delta t) \rangle = 0 \quad (21)$$

Accordingly, keeping in mind that the O-U process is a stationary process, the 2nd moments boil down to

$$\begin{aligned} \langle \mathcal{H}^2(0, \Delta t) \rangle &= \exp(-2\omega_{ac}\Delta t) \int_0^{\Delta t} \int_0^{\Delta t} d\tilde{s} d\tilde{s}' \exp(\omega_{ac}(\tilde{s} + \tilde{s}')) \langle \mathcal{L}(\tilde{s}) \mathcal{L}(\tilde{s}') \rangle \\ &= A \exp(-2\omega_{ac}\Delta t) \int_0^{\Delta t} d\tilde{s} \exp(2\omega_{ac}\tilde{s}) \\ &= \frac{A}{2\omega_{ac}} \{1 - \exp(-2\omega_{ac}\Delta t)\} \end{aligned} \quad (22)$$

The second moments of \mathcal{H} can be expanded in a closed form as in Eqn. (23).

$$\begin{aligned} \langle \mathcal{H}^2(0, \Delta t) \rangle &= \frac{\mathcal{A}}{2\omega_{ac}} \{1 - \exp(-2\omega_{ac}\Delta t)\} \\ &= \frac{\mathcal{A}}{2\omega_{ac}} \left[2(\omega_{ac}\Delta t) - 2(\omega_{ac}\Delta t)^2 + \frac{8}{3!}(\omega_{ac}\Delta t)^3 - \dots \right] \\ &= \mathcal{A}\Delta t \left[1 - \mathcal{R}_1 + \frac{2}{3}\mathcal{R}_1^2 - \frac{1}{3}\mathcal{R}_1^3 + \dots \right], \end{aligned} \quad (23)$$

with \mathcal{R}_1 being $\omega_{ac}\Delta t$. What determines the $\langle \mathcal{H}^2 \rangle$ is $\omega_{ac}\Delta t$, which is time step Δt in units of autocorrelation time τ_{ac} , not autocorrelation time, or time step by itself. This module is designed to generate O-U stochastic noise $\eta(t)$ that is to be applied to macroparticles in the form of magnetic-field perturbation: *autocorrelation time* (τ_{ac}), *time step* (Δt), and *noise strength* (\mathcal{A}).

B. Box-Muller-Like Transformation

The Box-Muller (BM) transformation [14, 15] is intrinsically for generating independent Gaussian white noise, which is a limiting case of physical noise, from independent uniform random deviates. In order to generate exponentially-driven Gaussian stochastic noise, an exponential factor, $\exp(-\omega\Delta t)$ is first multiplied by the stochastic noise $\eta(t)$ at present time t .

⁸ When a mean value of a variable is included in the moment calculation, it is referred to as *central moment*.

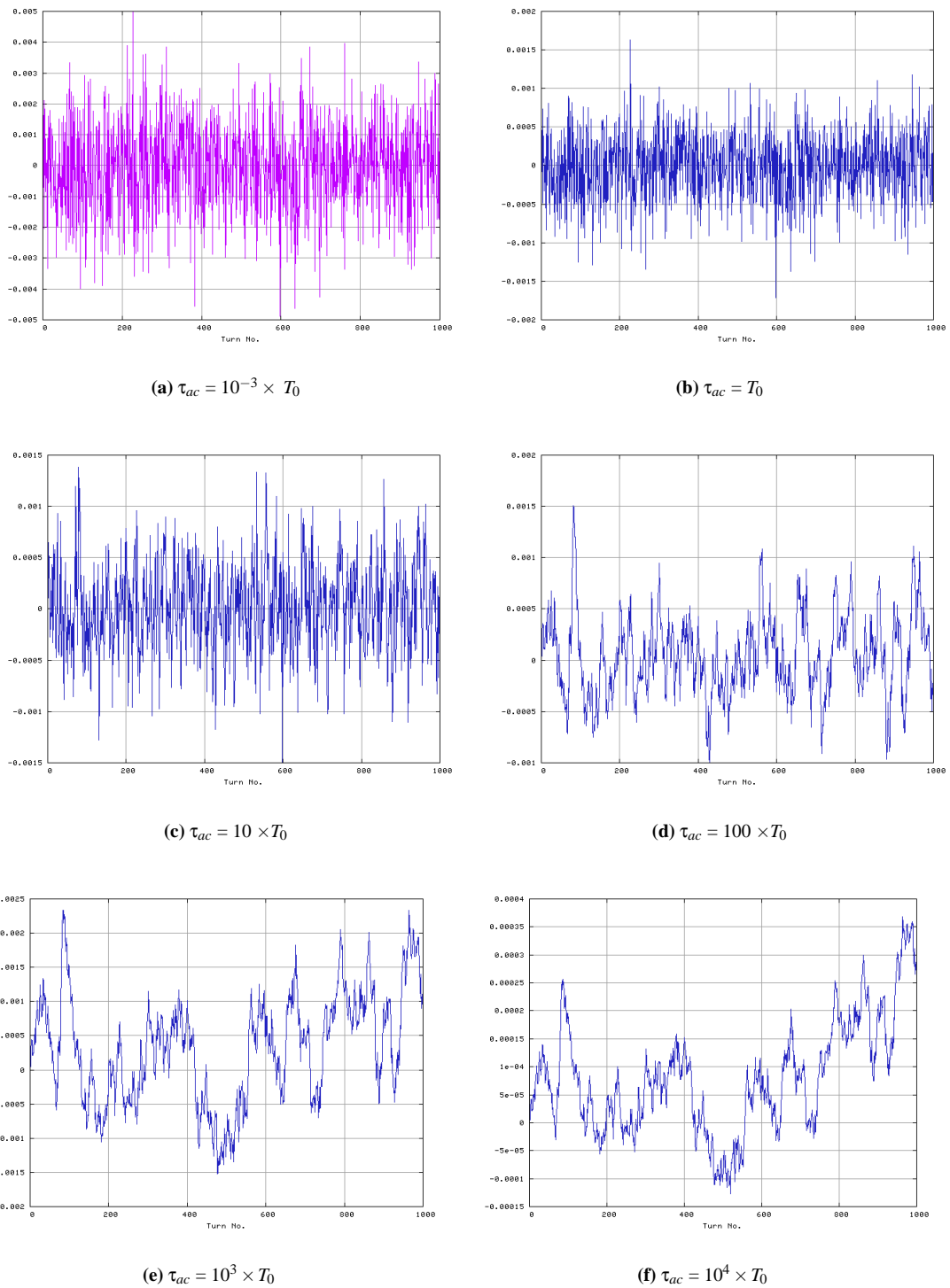


FIG. 4: Sample paths of the Ornstein-Uhlenbeck noise over 1,000 tracking turns; the autocorrelation time (τ_{ac}) ranges from $10^{-3} \times T_0$ to $10^4 \times T_0$, where T_0 denotes one revolution period.

Then, a root-mean-square (rms) value of $\mathcal{H}(0, \Delta t)$ is added to compute the noise at the next time step $t + \Delta t$.

$$\begin{aligned}\eta(t + \Delta t) &= \exp(-\omega\Delta t) \cdot \eta(t) + C_W \cdot \sqrt{\langle \mathcal{H}(t, t + \Delta t)^2 \rangle} \\ &= \exp(-\omega\Delta t) \cdot \eta(t) + C_W \cdot \sqrt{\langle \mathcal{H}(0, \Delta t)^2 \rangle},\end{aligned}\quad (24)$$

where C_W denotes random deviates from a rectangular distribution (or white noise). What Eqn. (24) implies is that to generate $\eta(t + \Delta t)$, one needs to know $\eta(t)$ only. This takes advantage of the powerful *Markov property* of the O-U process in numerical calculations. Upon providing with stochastic parameters, the variant of the BM transformation is capable of generating a wide spectra of stochastic noise: *colored noise*, *non-white noise*, *off-white noise*, etc. Sample paths are plotted in FIG. 4 with different autocorrelation time (τ_{ac}) ranging from $10^{-3} \times T_0$ (T_0 is one revolution period.) to $10^4 \times T_0$. The time step is fixed at one revolution period at the Booster injection energy. FIG. 4 demonstrates that the autocorrelation time governs the pattern of sample path. It is therefore evident that the pattern of all sample paths are *irregular* or *aperiodic*. More details of the non-white noise algorithm can be found elsewhere [16].

C. Application of Noise to Macroparticles

Since current fluctuations are directly proportional to magnetic-field fluctuations, in the noise model the ripple-current measurements are translated into magnetic-field fluctuations as in Eqn. (25).

$$\tilde{\mathbf{K}}_{imag} = \mathbf{K}_{imag} + \left| \Delta \mathbf{K}_{imag} \right| = \mathbf{K}_{imag} \cdot \left(1 + \left| \Delta \mathbf{K}_{imag} \right| / \mathbf{K}_{imag} \right), \quad (25)$$

where *imag* denotes magnet index for differentiating all 96 main magnets. In order to distinguish field fluctuations at each type of magnet (*F*, or *D*), \mathbf{K}_{imag} is factored out, and the amount of field variation ($\Delta \mathbf{K}_{imag}$) is normalized by \mathbf{K}_{imag} as a perturbation. It should be noted that according to experimental measurements (see section VII), the amount of ripple current (ΔI) is positive above the baseline of a sinusoidal current waveform. Hence, absolute values of $\Delta \mathbf{K}_{imag}$ ($\left| \Delta \mathbf{K}_{imag} \right|$) are taken as in Eqn. (25).

VI. GRADIENT-MAGNET POWER-SUPPLY (GMPS) SYSTEM

The Gradient Magnet Power Supply (GMPS) System for the Booster synchrotron powers a total of 96 main gradient magnets⁹. A resonance system is selected in order to reduce the size and the cost of the power-supply system. The

Booster magnet system consists of 48 LC-resonant magnet cells. A focusing magnet (F), a defocusing magnet (D), a choke, and a capacitor bank constitute an individual magnet cell. In turn, 48 focusing and 48 defocusing magnets are connected in series by common buses. Since the gradient magnets are powered by four independent power supplies (GMPS) that are symmetrically inserted in the LC-resonant system, the GMPS voltages to ground (V_{+G} and V_{-G}) can be kept as low as possible. Each GMPS drives current at the fundamental frequency of 15 Hz through a string of 12 magnet cells. The GMPS system includes dual three-phase Silicon Controlled Rectifier (SCR) bridges connected in series, and fed by a 12-phase 13.8-kV bus with shunt (or stray) capacitors connected to ground. The components of the Booster GMPS system are summarized in Table I.

TABLE I: The Booster Gradient-Magnet System

Component	No.
LC-resonant magnet cells	48
Focusing magnets	48
Defocusing magnets	48
Chokes	48
Capacitor Banks	48
GMPS	4
Gradient Magnets / cell	2
Choke / cell	1
Magnet cells / GMPS	12

VII. NOISE-MEASUREMENT TECHNIQUES AND ANALYSIS

A. Common-Mode Noise and Differential-Mode Noise

Starting from summer 2005 through winter 2006, we repeatedly conducted direct measurements of 15-Hz current on the main bus line and common-mode and differential-mode voltages at each of four GMPS. From a series of measurements, we confirmed that ripple current and common-mode voltages have been consistently detected and they are not of seasonal behavior at each individual GMPS unit. A 15-Hz current waveform over 3 cycles is shown in FIG. 5. Frequency and period of the current are shown in the shaded boxes on the figure. Two of four GMPS units located in the East Booster gallery are pictured in FIG. 6. As illustrated by FIG. 7, the waveforms of both V_{+G} and V_{-G} signals are sampled at the two leads on the GMPS control rack. Utilizing a digital oscilloscope,¹⁰ common-mode voltages and differential-mode

⁹ The gradient magnet is referred to as the combined-function magnet of the Booster.

¹⁰ The model name of the digital oscilloscope used for the measurements is Agilent 54622A, and the part number 54622-97014.

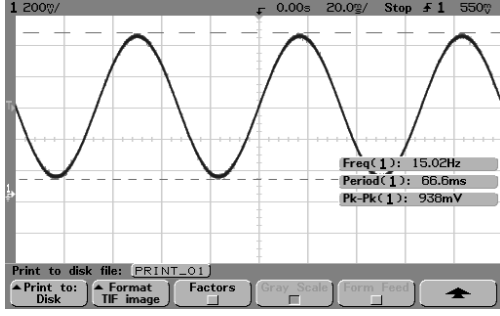


FIG. 5: 15-Hz current waveform taken at GMPS #1



FIG. 6: Two GMPS Units

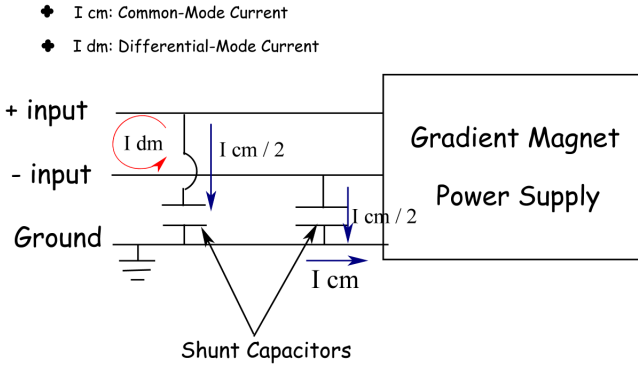


FIG. 7: Common-mode current and differential-mode current at the Booster GMPS

voltages are calculated as follows:

$$\begin{cases} V_{CM} = V_{+G} + V_{-G} \\ V_{DM} = V_{+G} - V_{-G} \end{cases} \quad (26)$$

FIG. 8 shows that the waveforms of V_{+G} and the inverted V_{-G} (\tilde{V}_{-G}) are overlaid for easy comparison on the same scale. In addition to FIG. 8, overlaid CM voltages are plotted against V_{+G} and \tilde{V}_{-G} at each GMPS in FIG. 9. Peak-to-peak measurements quantify the potential differences and cursor-key-function determines phase lags between two signals. Potential differences are displayed in FIG. 10. In principle, the waveforms of V_{+G} and V_{-G} are supposed to be 180 degrees out of

phase. However, as displayed in FIG. 11, substantial amounts of phase lag are found at each GMPS. We calculated the fractional difference in amplitudes ($|\Delta V/V|$) by taking the difference between V_{+G} and \tilde{V}_{-G} and normalizing the difference by V_{+G} . It was discovered that substantial amounts of potential differences in V_{+G} and V_{-G} are present at each GMPS unit. The counterparts of DM voltage are shown in FIG. 12. The DC output of the power supply is filtered with a L-C network, with the aid of a 15-Hz low-pass filter, to smooth the differential-mode sawtooth waveform at all GMPS units. The waveforms of CM voltage (V_{CM}) are noticeably fast fluctuating, which will induce additional current fluctuations in the system. Peak-to-peak amplitudes of V_{+G} and \tilde{V}_{-G} are plotted in FIG. 10. Phase lags between waveforms of V_{+G} and \tilde{V}_{-G} are plotted in FIG. 11. The voltage divisions are set to 500 mV/div and the sweep speed is set to 20 mV/div in FIG. 8 through FIG. 10. From these measurements, it was found that the mismatch of potential differences and phase lags between V_{+G} and V_{-G} for each GMPS unit are different.

It was found that the following are the two root causes of common-mode noise arising from each GMPS unit:

- (1) additional phase lags (ΔX) between V_{+G} and V_{-G}
- (2) amplitude (potential) difference between V_{+G} and V_{-G}

When V_{+G} and V_{-G} are added in a point-by-point fashion on the scope, they do not cancel each other. Instead, the ripples on each waveform add up and the common-mode voltage thus stands out.

The potential differences and the phase lags measured for individual GMPS units are summarized in Table II. Of four GMPS units, fractional potential difference in GMPS #2 is the largest and the worst. FIG. 13 shows the ripple current

TABLE II: Difference in voltage amplitudes and phase lags at each GMPS

GMPS No.	V_{+G} (V)	V_{-G} (V)	$ \frac{\Delta V}{V} $	ΔX (ms)
GMPS 1	1.577	1.905	20.8 %	0.6
GMPS 2	3.232	1.699	47.4 %	4.0
GMPS 3	1.598	1.740	8.9 %	1.4
GMPS 4	1.581	1.743	10.2 %	4.6

on a linear ramp of the sinusoidal waveform. The current are sampled directly from the magnet bus line. Since the ripple current are such a small fraction of the reference current, transductor electronics and a current amplifier (TA22 Texas Instruments) are used for signal amplification. FFT impulses of current waveform of one cycle is displayed in FIG. 15. The vertical scale is 20 dB/div and the horizontal span is 1,670 Hz.

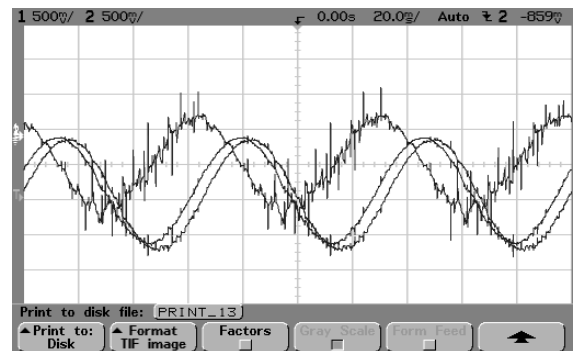
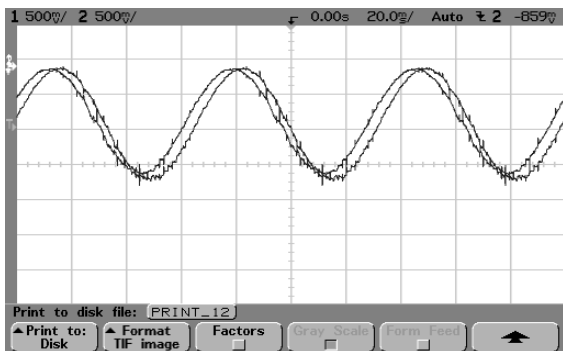
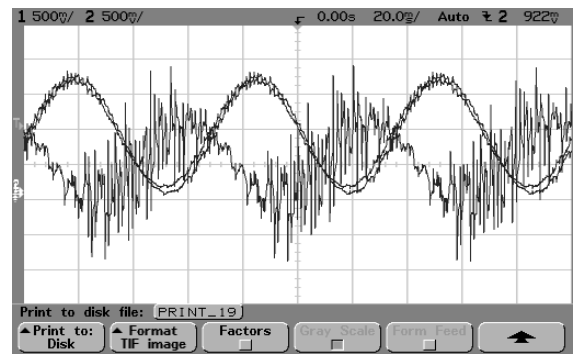
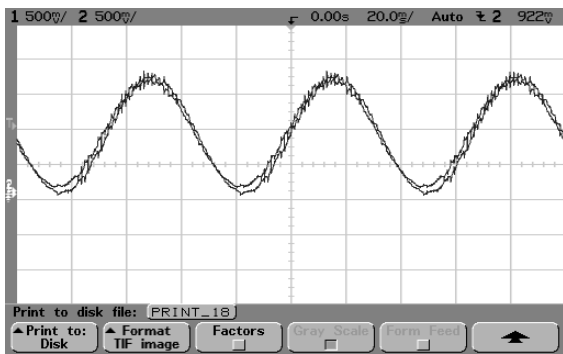
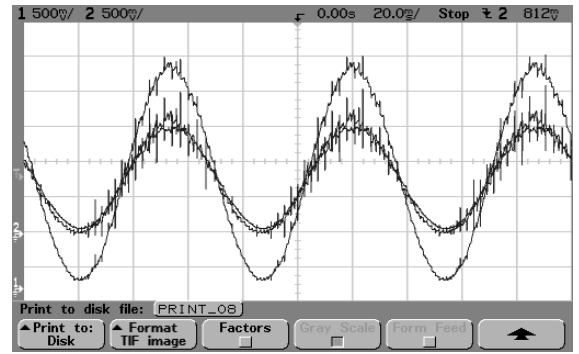
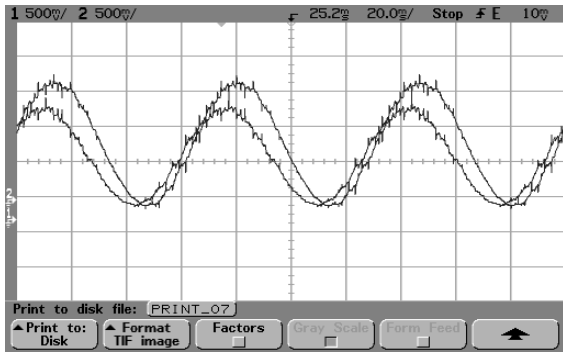
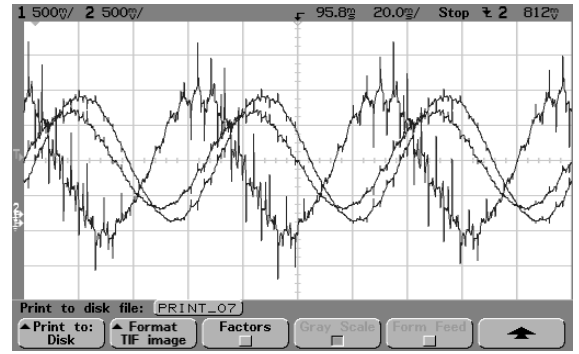
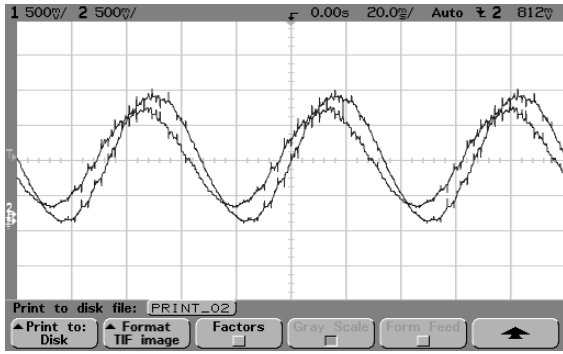
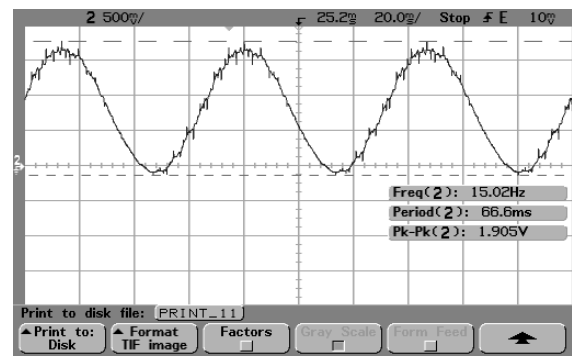
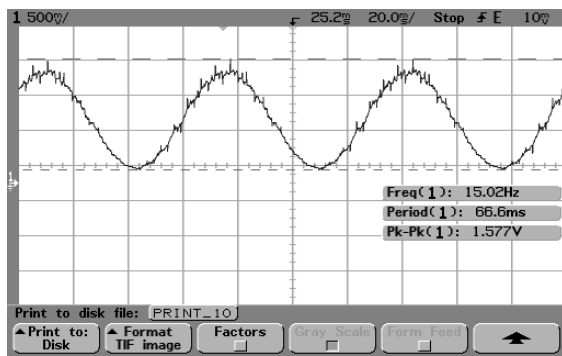
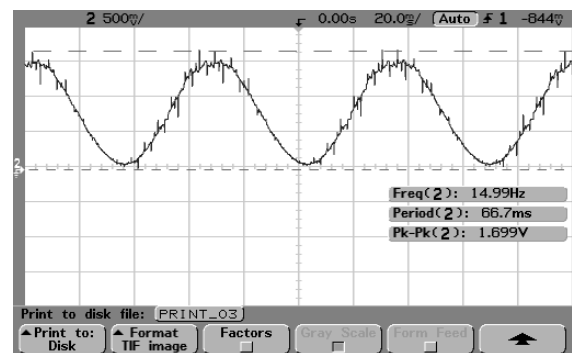
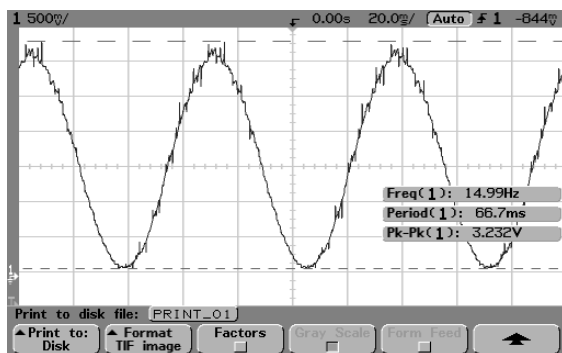


FIG. 8: The waveforms of V_{+G} and inverted V_{-G} . Progressing from top to bottom, each waveform shown on the oscilloscope display corresponds to GMPS #1 through GMPS #4. As indicated on the upper edge of each display, the voltage division is set to 500 mV/div and sweep speed to 20 ms/div.

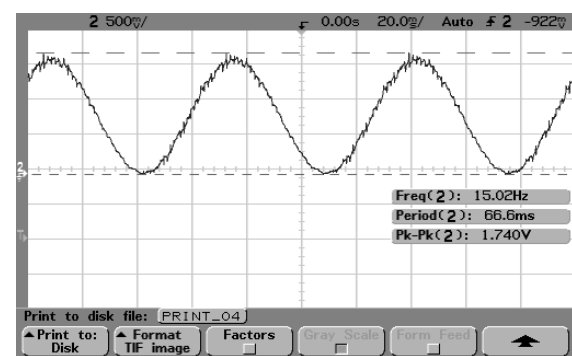
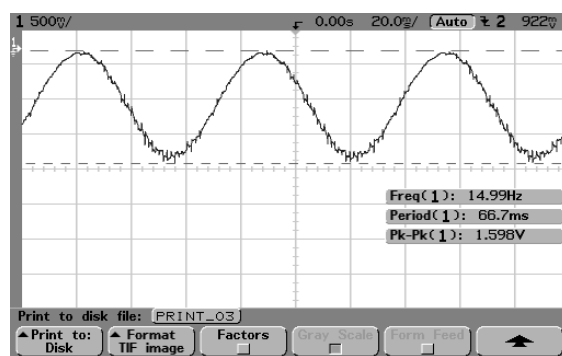
FIG. 9: The waveforms of V_{CM} are plotted against those of V_{+G} and inverted V_{-G} . Starting from top to bottom, each display corresponds to the GMPS #1 through the GMPS #4.



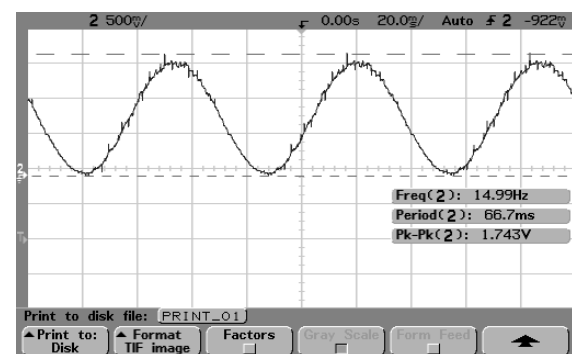
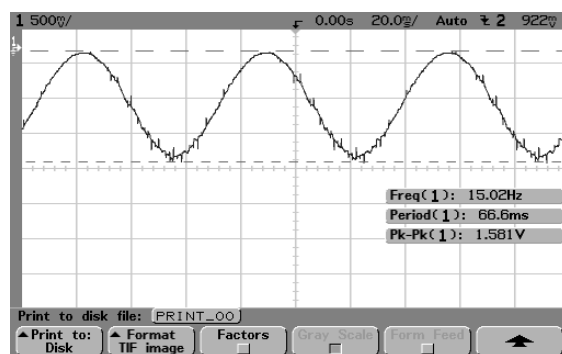
(a) GMPS #1



(b) GMPS #2

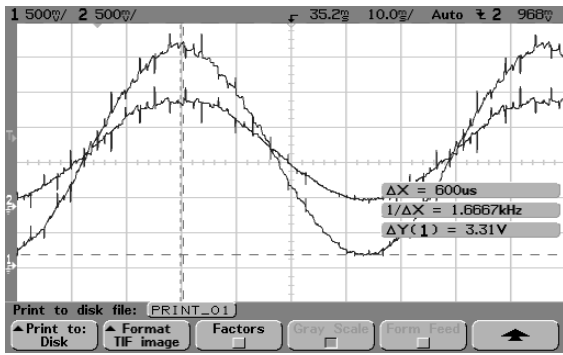


(c) GMPS #3

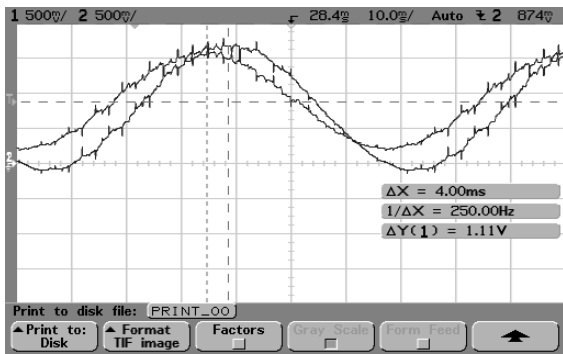


(d) GMPS #4

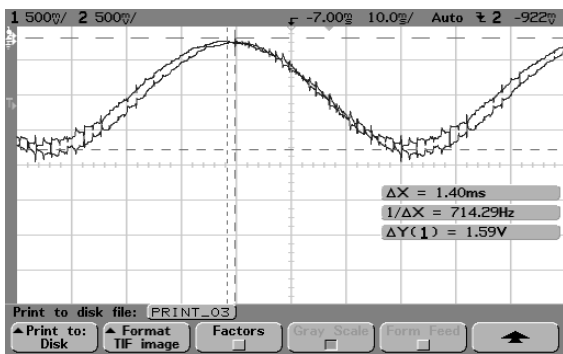
FIG. 10: Peak-to-peak amplitudes (Pk-Pk(1) and Pk-Pk(2)) and frequencies of V_{+G} and inverted V_{-G}



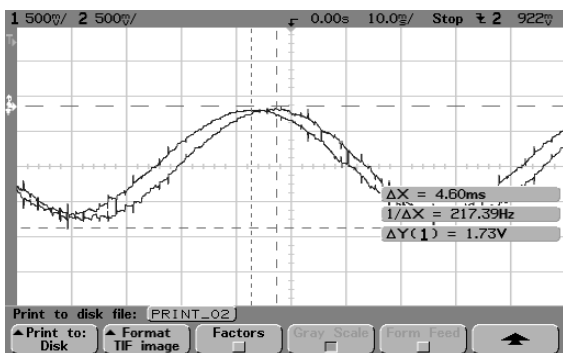
(a) [GMPS #1]: phase lag (ΔX) is 0.6 ms



(b) [GMPS #2] phase lag (ΔX) is 4.0 ms



(c) [GMPS #3] phase lag (ΔX) 1.40 ms



(d) [GMPS #4] phase lag (ΔX) 4.60 ms

FIG. 11: phase lags between V_{+G} and inverted V_{-G}

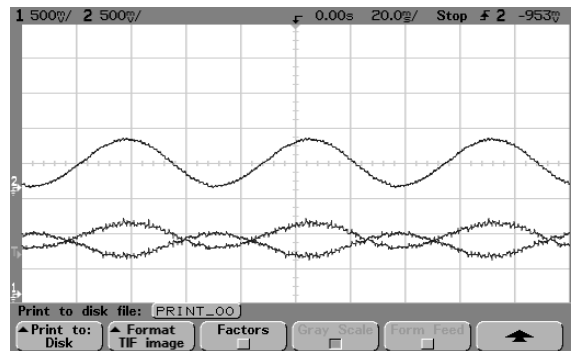
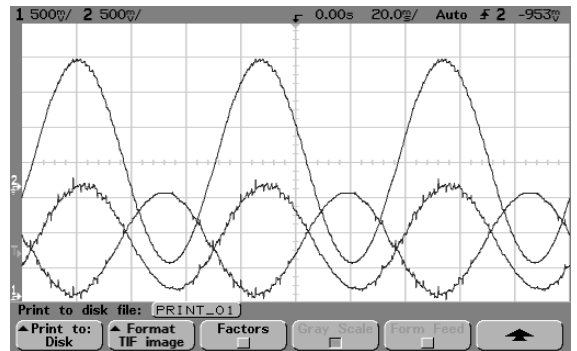
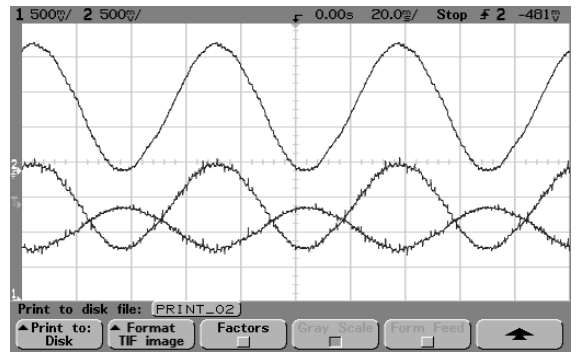
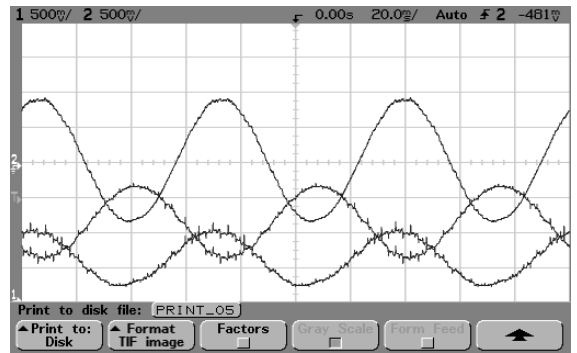


FIG. 12: The upper waveform is differential-mode voltage (V_{DM}) that are plotted against a pair of waveforms of V_{+G} and V_{-G} . Progressing from top to bottom, each plot corresponds to GMPS #1 through #4.

B. Power Spectral Density of Noise: FFT Analysis

The measured common-mode voltages from all of four GMPS units and the current signal with ripples are Fourier-analyzed. To provide *real-time* proof of the presence of offending interference in the power-supply system, all the signals are analyzed *on the fly* without being transported to any commercial software for the post-measurement analysis. We performed *real-time* analysis with the aid of the built-in FFT-function feature on the scope in use. The FIG. 5 through FIG. 13 are the real-time graphics saved on the scope. The resolution of a resonant peak, or FFT bin size, is determined by the FFT sampling rate and the number of points. The number of points on the scope is fixed at 2048, such that the FFT sampling rates and the span of the frequency domain are controlled in accordance with the Nyquist sampling theorem. In addition, in order to enhance spectrum resolution around the frequency peak, the *Hanning window* was selected over flat-top, rectangular, and Hamming windows. The selected Hanning-window function is given in Eqn. (27):

$$\mathcal{W}_H(t) = \frac{1}{2} \left[1 - \cos\left(\frac{2\pi \cdot t}{N-1}\right) \right], \quad (27)$$

in which $\mathcal{W}_H(t)$, t and N denote Hanning-window function, time, and the number of samples, respectively.

The following is a list of the FFT settings used on the scope:

- (1) FFT sampling rate, $f_s = 3.53$ kSa/s
- (2) FFT bin size, $\Delta f = 1.04$ Hz
- (3) Frequency-domain span = 1.67 kHz
- (4) Horizontal scale = 167 Hz/div
- (5) Vertical scale = 20 dB/div

According to the Nyquist sampling theorem, the oscilloscope determines FFT sampling rate from the chosen span of Frequency domain.

C. Parameterization of GMPS Noise

For stochastic noise models, the autocorrelation time τ_{ac} can be viewed as a memory span, or a measure of the dependence of the same stochastic values at two distinct times (t and t'). In this subsection, the measured current fluctuations are parameterized with the three stochastic parameters introduced in preceding sections IV and V:

- (1) **time step (Δt):** The entire Booster magnet system is divided into four quadrants. Each quadrant made up of a string of 24 magnets in series connection is driven by one GMPS. Current fluctuations ($\Delta I/I$) from each GMPS are transmitted to all magnets in each quadrant of the ring. As such, all of the 24 magnets experience the same amount of ripple current at an interval of the time step. Hence, the time step, or noise-sampling rate is chosen to be one revolution period ($T_0 = 2.2 \mu\text{s}$) at injection energy of 400

MeV.

- (2) **autocorrelation time, or correlation time (τ_{ac}):** On the basis of direct current measurements from a main bus line the ripple current are repeated above the base current, or reference current at an interval of $1.5 \sim 1.7$ (ms) (see FIG. 13). Therefore, about $1.5 \sim 1.7$ (ms) is chosen to be a proper autocorrelation time for additional ripple current originated from each GMPS.
- (3) **noise strength (\mathcal{A}):** Based upon the amplitudes of ripple current ($\Delta I/I$) on a linear ramping portion of a sinusoidal current waveform (cf. FIG. 13), the rms value of fractional current fluctuation $\Delta I/I|_{rms}$ is on the order of 10^{-4} . For verification purpose, histograms of the O-U noise generated from each of four noise nodes that are symmetrically inserted around the Booster ring are plotted. As shown in FIG. 14, the rms values of histograms are on the same order as those of measured noise strengths.

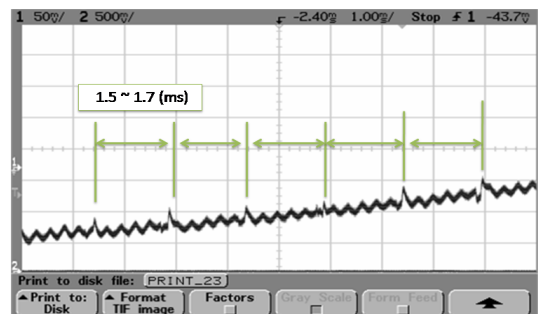


FIG. 13: ripple current on a linear ramp of the sinusoidal waveform. The current are sampled directly from the magnet bus line.

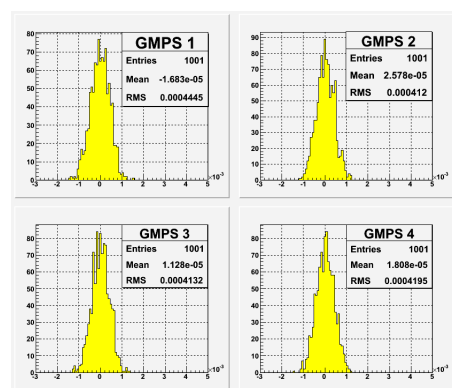


FIG. 14: Histogram of the amplitudes of noise generated at each random noise node.

The autocorrelation function of a signal, or the power spectra can be measured by means of FFT.

$$S_{\xi}(\omega) = \frac{1}{2\pi} \int_{-\infty}^{\infty} e^{-i\omega\tau} C_{\xi}(\tau) d\tau \quad (28)$$

$$C_{\xi}(\tau) = \int_{-\infty}^{\infty} e^{i\omega\tau} S_{\xi}(\omega) d\omega \quad (29)$$

According to the Wiener-Khinchine theorem [4], spectral density is the Fourier transform of the autocorrelation function $C_{\xi}(\tau) = \langle \xi(\tau)\xi(t + \tau) \rangle$ for stationary processes:

$$S_{\xi}(\omega) = 2 \int_0^{\infty} \langle \xi(\tau)\xi(t + \tau) \rangle \cos(\omega\tau) d\tau, \quad (30)$$

with $S_{\xi}(\omega)$ being spectral density of a stochastic process ξ . In FIG. 15, FFT is performed with one-cycle range of time data from 15-Hz current. For FIG 15 (a), the horizontal scale is 167 Hz/div, and the vertical scale is 20 dB/div. For FIG. 15 (b), the vertical scale is 10^{-1} to indicate power attenuation from 1.0. The power spectral density of the O-U noise is matched to that of the measured ripple current shown in FIG. 13.

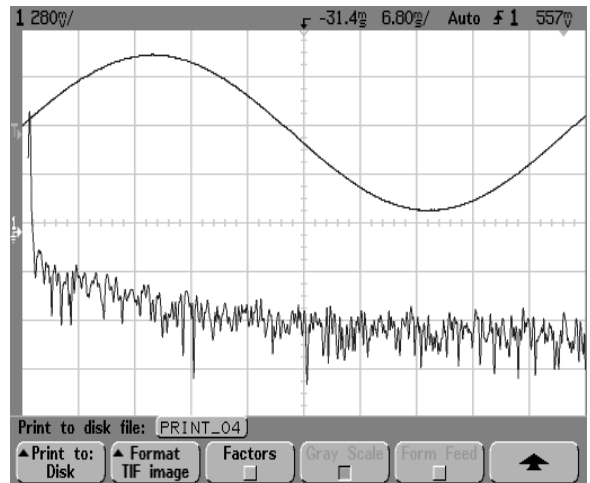
D. Equivalent-Circuit Model

To find out whether there are any offending resonances floating around the Booster magnet system, acting as noise amplifiers, the equivalent circuit modeling was also carried out. Since a string of 24 magnets in a quadrant of the Booster magnet system are connected in series, they are treated as one transmission line. We employed the B² SPICE [17] A/D Version 4, which is one of many versions of commercial SPICE simulators. FIG. 16 shows the results of AC analysis of the equivalent circuits. The current is peaked at 15 Hz and a cluster of minor peaks are found in a few kHz range. It is suspected that the offending resonances above 15 Hz, in higher frequency region, could amplify the offending noise, when the noise frequencies coincide with those of resonances. The presence of the resonances could augment the formation of beam halo, eventually resulting in beam loss.

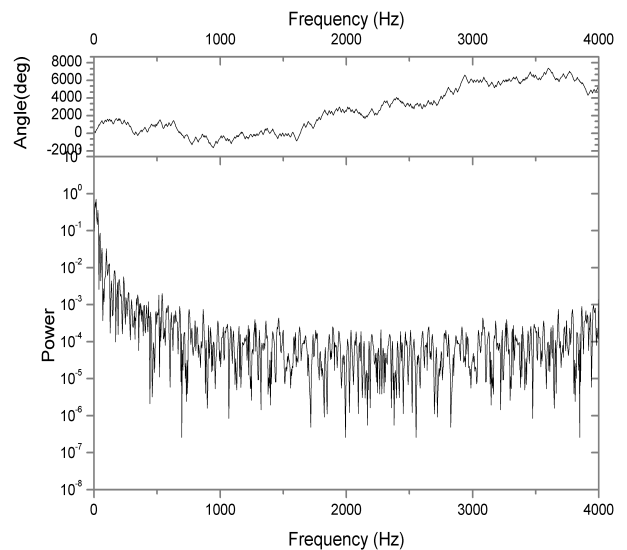
VIII. TRACKING AND BEAM DIAGNOSIS

A. Simulation Parameters

A comprehensive set of machine parameters for the Booster ring at injection energy is given in Table III. Some parameters listed in Table III are derived from lattice parameters specified in the Booster design lattice (version 1.1). Salient ORBIT-FNAL simulation parameters including space-charge calculations are listed in Table IV. A round beam with axisymmetry is first injected into the Booster ring before tracking. This ensures that we can solely investigate the noise effects under space charge alone. Optics functions ($\alpha(z)$, $\beta(z)$,



(a) ripple current



(b) Ornstein-Uhlenbeck noise

FIG. 15: (a) FFT impulses and 15-Hz current waveform of one cycle; the horizontal scale is 167 Hz/div and the vertical scale is 20 dB/div. (b) The power spectral density of the Ornstein-Uhlenbeck noise is matched close to that of measured ripple current

$\gamma(z)$, $\delta(z)$) are computed with the Booster design lattice using MAD (version 8.23) prior to particle tracking. According to the latest measurements and actual machine operation parameters, a careful choice of the other simulation parameters are made.

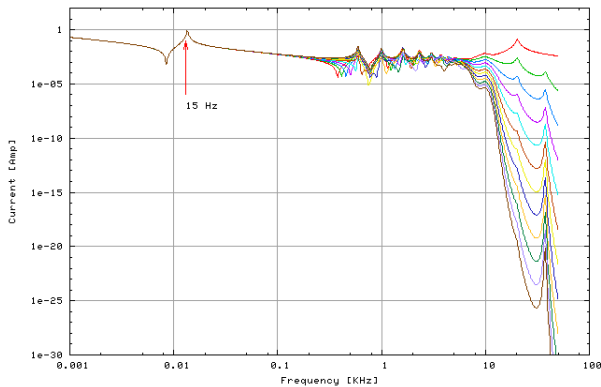


FIG. 16: [SPICE simulation]: Current vs. Frequency: current flowing through a string of 12 magnet cells driven by one GMPS. Progressing from top to bottom, the lines correspond to magnet cell [1] through magnet cell [12].

B. Parallelized Calculations

With fixed space-charge bin numbers of $(64 \times 64) \times 32$, rms emittances from tracking different numbers of macroparticles are calculated. As illustrated by FIG. 17, when the total number of macroparticles amounts to above 330,000, after injection is complete, the values of rms emittance converge with stability. Therefore, considering computation time and the number of macroparticles assigned to each space-charge bin, we determine that 330,000 macroparticles are adequate for investigation. Hence, each macroparticle represents $O(10^5)$ real particles, or protons in the noise model. In order to facilitate tracking of a large number of macroparticles, additional beam diagnostic calculations are implemented in *parallel* mode.

C. Moments

In the following subsections, we will present how beam diagnostic quantities are defined and computed for the stochastic noise model. we define moments which characterize probability distributions of a beam, or macroparticles. Since it is necessary to consider beam centroids ($\langle x \rangle$ and $\langle y \rangle$), ORBIT-FNAL employs central moments in the calculations:

$$\begin{cases} \Delta x_r &= x_r - \langle x_r \rangle \\ \Delta y_r &= y_r - \langle y_r \rangle \end{cases} \quad (31)$$

Because of vanishing central moment calculation, beam centroids themselves ($\langle x \rangle$ and $\langle y \rangle$) are used for the 1st moment calculations. It is assumed that the density profiles of an actual beam in transverse planes are *bi-Gaussian*. We first injected macroparticles of bi-Gaussian distribution. Then, rms beam

TABLE III: Machine Parameters of Fermilab's Booster at Injection Energy

ring radius ($\langle R \rangle$)	75.47 (m)
ring circumference	474.2 (m)
injection kinetic energy	400 (MeV)
injection momentum	954.263 (MeV/c)
synchronous energy (E_s)	1.328 (GeV)
β (Lorentz factor)	0.7131
γ (Lorentz factor)	1.426
revolution period (T_0)	2.2 (μ s)
revolution frequency (f_0)	454.5 (kHz)
no. of injection turns	11
injection period	24.2 (μ s)
cycle time	66.7 (ms)
γ_{tr} (transition gamma)	5.4696
α_1 (momentum compaction factor)	0.0172
phase-slip factor ($ \eta $)	0.458
$\epsilon_{tr, 95, n}$ (95 %, normalized)	12.0 (π -mm-mrad)
RF Range	38.18 ~ 52.83 (MHz)
v_x/v_y (bare tunes)	6.7 / 6.8
betatron frequency ($f_{\beta,x}, f_{\beta,y}$)	318.2 / 363.6 (kHz)
Q_s (synchrotron tune)	1.147×10^{-3}
Ω_s (synchrotron frequency)	3.28 (kHz)
T_s (synchrotron period)	305 (μ s)
β_s (longitudinal beta function)	3.0×10^4 (m)
ϵ_l (longitudinal emittance)	0.25 (eV-s)
batch intensity	5.04×10^{12}
average beam current at injection	420 (mA)
effective beam radius	0.0325 (m)
effective beam-pipe radius	0.0653 (m)
bunching factor (B_f)	~ 0.4
$\frac{\Delta P}{P_0} _{max}$	± 0.15 %
σ_δ	3.0×10^{-4}
$\beta_{x,max} / \beta_{y,max}$	33.7 / 20.5 (m)
$D_{x,max} / D_{y,max}$	3.2 / 0.0 (m)
cell type	FOFDOOD
cell length	20.62 (m)
gradient magnets / cell	4
total gradient magnets	96
$V_{rf, inj}$ (RF voltage at injection)	205.0 (kV/Turn)
phase advance / cell	96 (deg)
ρ_D (defocusing bending radius)	48.034100 (m)
ρ_F (focusing bending radius)	40.847086 (m)

sizes (σ_x, σ_y) are calculated from the 2nd moment calculation:

$$1^{st} \text{ moments } \begin{cases} \langle x_r \rangle \\ \langle y_r \rangle \end{cases} \quad (32)$$

$$2^{nd} \text{ moments } \begin{cases} \sigma_x^2 &= \langle (\Delta x_r)^2 \rangle \\ \sigma_y^2 &= \langle (\Delta y_r)^2 \rangle \end{cases} \quad (33)$$

TABLE IV: Salient Booster Simulation Parameters with ORBIT-FNAL

no. of injection turns	11
no. of maximum macroparticles	330,000
harmonic no.	84
beam kinetic energy	400.0 (MeV)
beam intensity (per RF bucket)	6.0×10^{10}
transverse beam distribution	bi-Gaussian
ring circumference	474.2 (m)
$\beta_{x, inj} \beta_{y, inj}$	6.274 / 19.312 (m)
$\alpha_{x, inj} \alpha_{y, inj}$	-0.122 / 0.024
$D_{x, 0} D_{y, 0}$	2.581 / 0.0 (m)
$x_0, inj y_0, inj$	0.0 / 0.0 (mm)
E_{offset}	0.0 (GeV)
$\Delta E / E_{kinetic}$	5.1×10^{-4}
$\epsilon_{x, rms, inj} \epsilon_{y, rms, inj}$	1.76 / 1.76 (π -mm-mrad)
V_{rf} (RF voltage)	205.0 (kV/Turn)
R_{wall} / R_{beam} (for geometric factor)	2.0
longitudinal SC bin no.	32
transverse SC bin no.	64 x 64
smoothing parameter	$\sim 10^{-4}$
no. of total tracking turns	1,000

^aLSC stands for longitudinal space charge.

^bTSC stands for transverse space charge.

The rms beam sizes are important for space-charge study in that those are the contributing factors of transverse space-

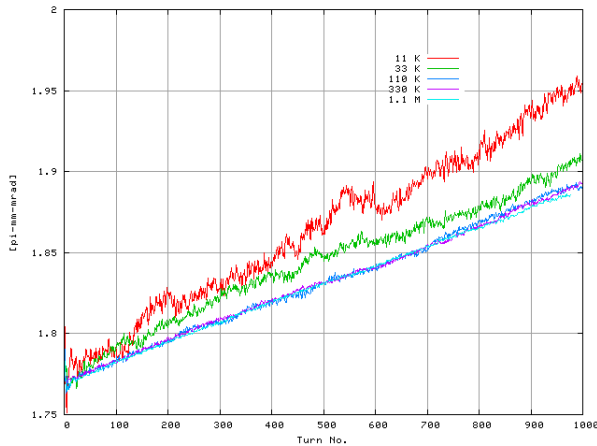


FIG. 17: Calculations of rms emittances with a varying number of total macroparticles and fixed space-charge bin numbers; progressing from top to bottom, each trace corresponds with 11,000, 33,000, 110,000, 330,000, and 1,100,000 macroparticles in total.

charge forces as described below:

$$\begin{cases} F_x & \propto \frac{\lambda}{\gamma^2} \cdot \frac{1}{\sigma_x(\sigma_x + \sigma_y)} \\ F_y & \propto \frac{\lambda}{\gamma^2} \cdot \frac{1}{\sigma_y(\sigma_x + \sigma_y)}, \end{cases} \quad (34)$$

where λ and γ are charge density and relativistic factor, respectively. To understand the time evolution of rms beam sizes, or rms beam widths in transverse planes, the 2nd moments in real physical space are computed.

The injection transverse coordinates employed in the ORBIT-FNAL are defined in physical space as a function of azimuthal coordinate z . Hence, the horizontal coordinates include the effects of horizontal dispersion ($\mathcal{D}_{x0}(z)$). On the other hand, no dispersion effect is included in the vertical coordinates because vertical dispersion ($\mathcal{D}_{y0}(z)$) is set to zero in accordance with the Booster design lattice. Consequently, the following relations are implicitly reflected in the macroparticle coordinates and the calculations of transverse rms emittances:

$$\begin{cases} x_r(z) & = x_\beta(z) + D_x(z) \cdot \frac{\Delta p}{p_0} \\ y_r(z) & = y_\beta(z) \end{cases} \quad (35)$$

In Eqn. (35), $x_r(z)$ and $y_r(z)$ denote real-space coordinates, and $x_\beta(z)$ and $y_\beta(z)$ denote betatron coordinates, and $D_{x0}(z)$ and P_0 denote injection horizontal dispersion and design momentum, respectively. In a similar fashion, divergence angles are computed:

$$\begin{cases} x'_r(z) & = x'_\beta(z) + D'_x(z) \cdot \frac{\Delta p}{p_0} \\ y'_r(z) & = y'_\beta(z), \end{cases} \quad (36)$$

where $D'_x(z)$ denotes the slope of horizontal dispersion.

D. RMS Emittances

As the ORBIT-FNAL employs the 2nd-order central moments in the rms emittance calculations, we need to define additional quantities below to define rms emittances.

$$\begin{cases} \Delta \mathcal{P}_x & \equiv \mathcal{P}_x - \langle \mathcal{P}_x \rangle \\ \Delta \mathcal{P}_y & \equiv \mathcal{P}_y - \langle \mathcal{P}_y \rangle \end{cases} \quad (37)$$

In case of the synchrotron motion, $\Delta E (= E - E_s)$ of energy offset from synchrotron energy (E_s) and ϕ representing RF phase are used.

$$\begin{cases} \tilde{E} & \equiv E / (\omega_{rf}) \\ \Delta \tilde{E} & \equiv \tilde{E} - \tilde{E}_s \\ \delta \tilde{E} & \equiv \Delta \tilde{E} - \langle \Delta \tilde{E} \rangle \\ \Delta \phi & \equiv \phi - \langle \phi \rangle, \end{cases} \quad (38)$$

with ω_{rf} being angular rf frequency. Note that the normalization factor of $1/(\omega_{rf})$ is introduced to transform synchrotron

(or longitudinal) coordinates into a pair of canonical conjugate coordinates (\tilde{E}, ϕ) . Once we define the 2^{nd} -order central moments of each coordinate in the 6-dimensional space, we define column matrices $\mathcal{M}_{2,x}$ and $\mathcal{M}_{2,y}$.

$$\mathcal{M}_{2,x} = \begin{bmatrix} \Delta x_\beta \\ \Delta x'_\beta \end{bmatrix} \quad \mathcal{M}_{2,y} = \begin{bmatrix} \Delta y_\beta \\ \Delta y'_\beta \end{bmatrix} \quad (39)$$

With the column matrices \mathcal{M}_2 above, we can define 2×2 Σ -matrices in subspaces of trace space: (x_β, x'_β) and (y_β, y'_β) . In each of Σ -matrices, the off-diagonal elements are associated with the correlation between position and angle, or energy and rf phase.

$$\begin{aligned} \Sigma(x_\beta, x'_\beta) &\equiv \langle \mathcal{M}_{2,x} \mathcal{M}_{2,x}^T \rangle \\ &= \begin{bmatrix} \langle (\Delta x_\beta)^2 \rangle & \langle \Delta x_\beta \Delta x'_\beta \rangle \\ \langle \Delta x'_\beta \Delta x_\beta \rangle & \langle (\Delta x'_\beta)^2 \rangle \end{bmatrix} \end{aligned} \quad (40)$$

in which \mathcal{M}^T denotes a transpose matrix of \mathcal{M} . Using the 2×2 Σ -matrix, an *unnormalized rms emittance* can be defined as,

$$\begin{aligned} \varepsilon_{x,rms} &= \sqrt{\det \Sigma(x_\beta, x'_\beta)} \\ &= \sqrt{\langle (\Delta x_\beta)^2 \rangle \langle (\Delta x'_\beta)^2 \rangle - \underbrace{\langle \Delta x_\beta \Delta x'_\beta \rangle^2}_{\text{correlation term}}} \end{aligned} \quad (41)$$

Transverse rms emittances are defined in $(x_\beta, \mathcal{P}_x/P_0)$ and $(y_\beta, \mathcal{P}_y/P_0)$ phase spaces, following the MAD [18] convention:

$$\Sigma(x_\beta, \mathcal{P}_x) = \begin{bmatrix} \langle (\Delta x_\beta)^2 \rangle & \langle \Delta x_\beta \Delta \mathcal{P}_x \rangle \\ \langle \Delta \mathcal{P}_x \Delta x_\beta \rangle & \langle (\Delta \mathcal{P}_x)^2 \rangle \end{bmatrix} \quad (42)$$

$$\begin{aligned} \varepsilon_{x,rms} &= \frac{1}{\mathcal{P}_0} \sqrt{\det \Sigma(x_\beta, \mathcal{P}_x)} \\ &= \frac{1}{\gamma \beta m_0 c} \sqrt{\langle (\Delta x_\beta)^2 \rangle \langle (\Delta \mathcal{P}_x)^2 \rangle - \langle \Delta x_\beta \Delta \mathcal{P}_x \rangle^2}, \end{aligned} \quad (43)$$

in which the transverse momenta (\mathcal{P}_x and \mathcal{P}_y) are normalized by the design momentum (\mathcal{P}_0). As stated earlier, if a unnormalized rms emittance is multiplied by the Lorentz factors ($\beta\gamma$), it transforms into a normalized rms emittance with no momentum dependence. The Eqns. (39) through (43) apply likewise to vertical and longitudinal planes.

$$\left\{ \begin{aligned} \varepsilon_{x,n,rms} &= (\beta\gamma) \varepsilon_{x,rms} \\ &= (\beta\gamma) \sqrt{\langle (\Delta x_\beta)^2 \rangle \cdot \langle (\Delta x'_\beta)^2 \rangle - \langle \Delta x_\beta \Delta x'_\beta \rangle^2} \\ &= \frac{1}{m_0 c} \sqrt{\langle (\Delta x_\beta)^2 \rangle \langle (\Delta \mathcal{P}_x)^2 \rangle - \langle \Delta x_\beta \Delta \mathcal{P}_x \rangle^2} \\ \varepsilon_{y,n,rms} &= (\beta\gamma) \varepsilon_{y,rms} \\ &= (\beta\gamma) \sqrt{\langle (\Delta y_\beta)^2 \rangle \langle (\Delta y'_\beta)^2 \rangle - \langle \Delta y_\beta \Delta y'_\beta \rangle^2} \\ &= \frac{1}{m_0 c} \sqrt{\langle (\Delta y)^2 \rangle \langle (\Delta \mathcal{P}_y)^2 \rangle - \langle \Delta y \Delta \mathcal{P}_y \rangle^2} \end{aligned} \right. \quad (44)$$

IX. IMPACT OF GMPS CURRENT FLUCTUATIONS WITH SPACE CHARGE

After inserting a total of four random-noise nodes, provided with characteristic stochastic noise parameters, into a Booster ring, macroparticles representing the Booster beams are tracked over 1,000 turns in the presence of full space charge¹¹. FIG. 18 shows that the time evolution of transverse rms emittances with the O-U noise¹² coupled to the full space-charge effects (red) and with the space-charge effects alone (blue). To estimate the emittance growth rate, the relative emittance growths $(\frac{\Delta \varepsilon}{\varepsilon_0})$ ¹³ are calculated starting from the last injection turns (the 11th turn) through 1,000th turn, prior to the beam acceleration; this corresponds to the first 2 ms of one cycle over 66.7 ms (15 Hz). In the horizontal plane the relative emittance growth is about 7.5 %, and in the vertical plane the growth is 9.3 %. A total of 330,000 macroparticles, or 30,000 macroparticles per each injection turn are simulated and tracked.

Upon including O-U noise representing GMPS noise, the process of beam degradation develops, and a more noticeable halo formation is found. As a cross-check with the rms emittance calculations, we also compute average actions at each tracking turn including the noise and the full space-charge effects. The rms emittances and average actions are overlaid in FIG. 19 for clear comparison. The calculations of both rms emittances and actions manifest in such a good agreement that beam degradation is substantially enhanced due to *synergistic mechanism* between GMPS-current fluctuations and space-charge effects. Here, we use the term *synergistic mechanism* meaning that the total effects of GMPS noise and space charge are larger than the sum of individual effects. The time evolution of rms beam sizes in both transverse planes with space charge alone and with noise and space charge are illustrated in FIG. 20. When the noise is included, the 2^{nd} moments, which is beam size squared, grow faster than in the case for space charge alone. If we lower the Booster batch intensity by an order of one magnitude (5×10^{11}) from the present operational batch intensity under the same conditions, the emittance growths induced by the GMPS noise and space-charge effects are not distinguishable from those of noise alone in the absence of space charge as shown in FIG. 21. It should be noted that the space-charge effect is intensity dependent. Thus, if the beam intensity is lowered, so is the space-charge effects. This is a clear signature that only when the space-charge effects are substantial, so does the GMPS noise have a substantial impact on the Booster beam. In addition to the primary beam diagnostic calculations of the rms emittances and average actions, we looked into the transverse couplings as well in the next subsection.

¹¹ Full space charge is referred to as both transverse and longitudinal space charge, or 3-D space charge

¹² Hereafter, the O-U noise means the stochastic noise modeled on the GMPS noise measurements.

¹³ ε_0 denotes initial emittance, and $\Delta \varepsilon = |\varepsilon - \varepsilon_0|$

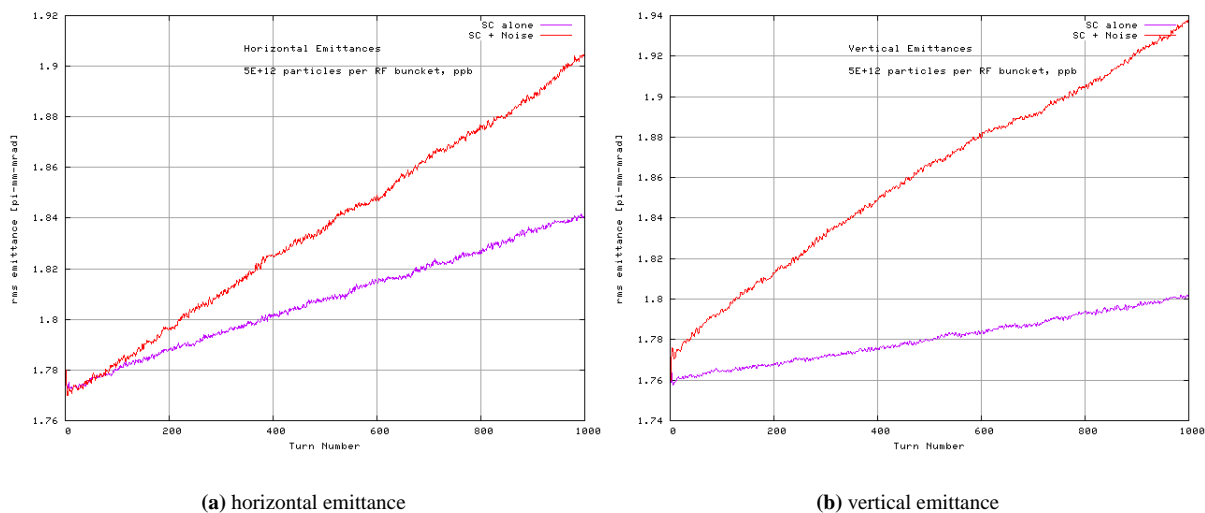


FIG. 18: transverse rms emittance growths starting from the outset of injection through 1,000 tracking turns, or prior to ramping; the noise and space-charge effects in red and the space-charge effects alone in blue. The beam intensity per bucket is 6.0×10^{10} ppb, and the batch intensity is 5.0×10^{12} protons.

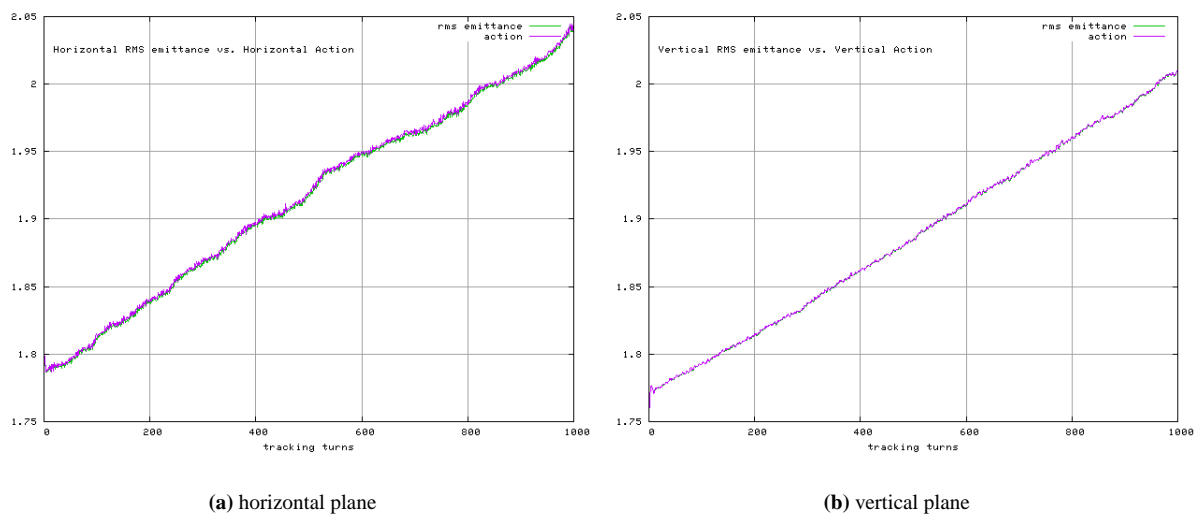


FIG. 19: Time evolution of rms emittances in comparison with actions; (a) horizontal rms emittance vs. horizontal action; (b) vertical rms emittance vs. vertical action

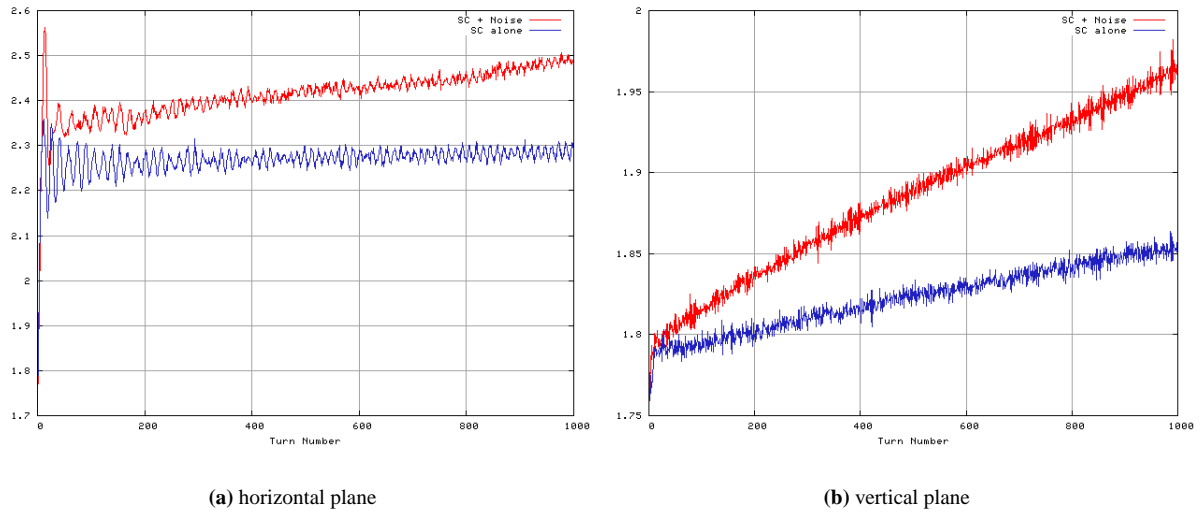


FIG. 20: Time evolution of 2^{nd} moments in transverse planes; space charge alone (blue) and space charge with noise (red)

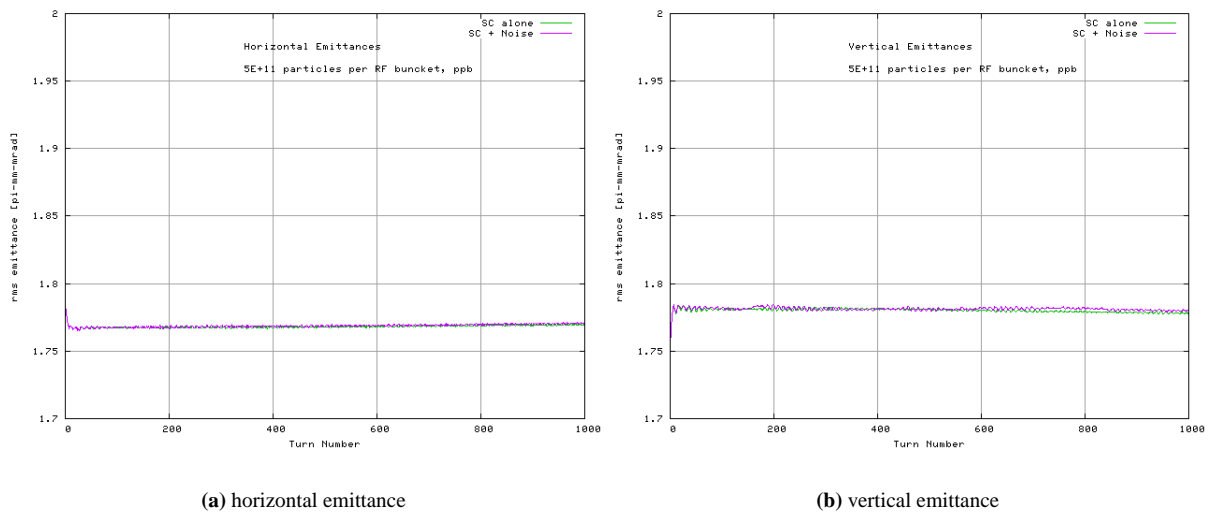


FIG. 21: transverse emittance growths; the noise and space-charge effects in red and the space-charge effects alone in blue. The beam intensity is 6×10^9 ppb, and 5×10^{11} protons in total.

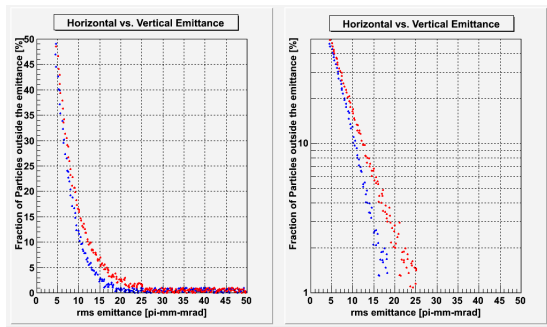


FIG. 22: Fractional exclusion of macroparticles at a given average action. The blue indicates at the 1st turn and the red indicates after 1,000 turns. The vertical axis on the left plot is in linear scale, and the right is on logarithmic scale.

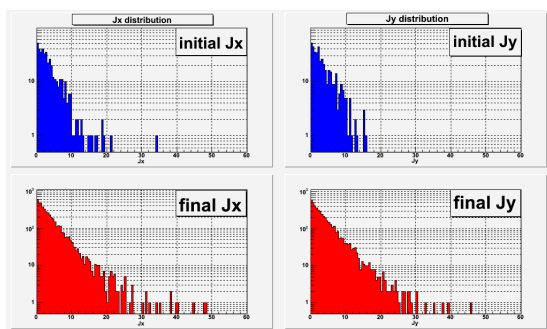
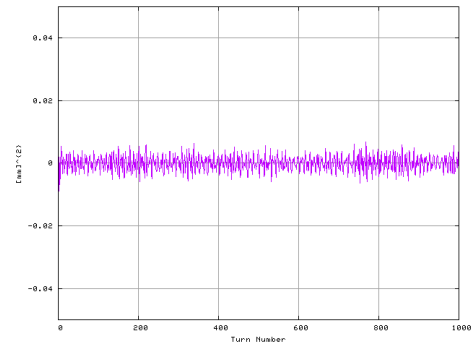


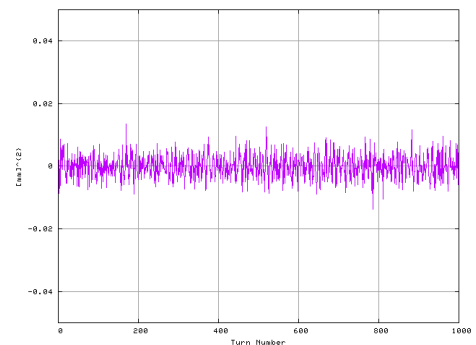
FIG. 23: The distribution of actions (J_x and J_y) at the 1st turn and after 1,000 turns. O-U noise and 3-D space-charge effects are included. Action distribution at the 1st turn is in blue, and action distribution after 1,000 turns in red.

A. Couplings

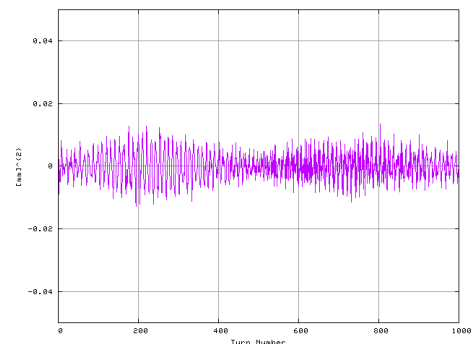
The computations of the 2nd-order cross moment $\langle xy \rangle$ for each case are presented in FIG. 24. A marginal amount of couplings are introduced due to the full space-charge effects (FIG. 24 (b)). When the noise is included alone in the absence of the space charge, couplings are somewhat noticeable (FIG. 24 (c)). When the noise and the full space-charge effects are included, the transverse couplings are substantially amplified. We therefore conclude that the noise impact on a beam is dependent upon the strengths of the space-charge defocusing forces in the Booster. What FIG. 22 illustrates is the percentage of macroparticles that reside outside of a given average action including the O-U noise and space charge. The blue markers indicate the fraction of excluded macroparticles at a given emittance at the 1st turn and the red markers at the end of tracking after 1,000 turns.



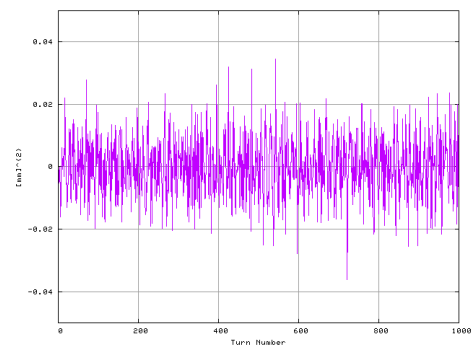
(a) $\langle xy \rangle$: No space charge; no noise



(b) $\langle xy \rangle$: Space charge alone



(c) $\langle xy \rangle$: Noise alone



(d) $\langle xy \rangle$: Noise coupled to space charge

FIG. 24: Transverse couplings in configuration space

FIG. 23 compares the distributions of transverse single-particle actions (J_x and J_y) at the outset of injection and at the end of 1,000 turns. It is evident that noise-induced beam degradation is enhanced as the time elapses.

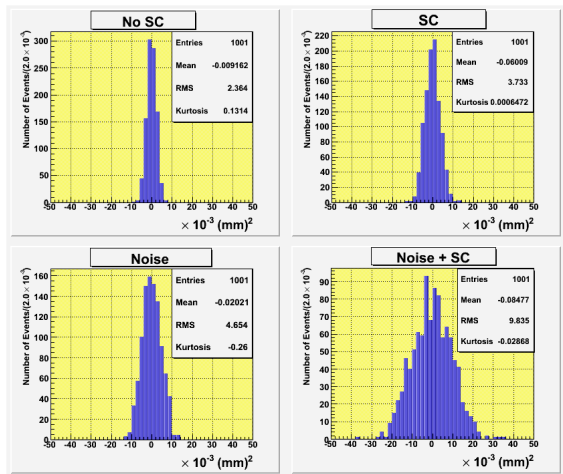


FIG. 25: The distributions of the magnitudes of the 2^{nd} -order cross moment ($\langle xy \rangle$)

B. Coupling Magnitude

In an ideal system the normalized rms emittance remains constant. However, nonlinear space-charge effect and couplings can induce degradation in beam quality. The increases of the normalized rms emittances indicate that nonlinear space-charge effect and couplings induced by different machine imperfections are present in the Booster. One of the great advantages of the realistic accelerator simulation with macroparticle tracking is that we can isolate an accelerator system condition to narrow down a specific cause of emittance growth under investigation. Therefore, in order to look into the transverse couplings, we additionally implemented in the ORBIT-FNAL new parallelized calculations of 4-dimensional transverse emittances (ϵ_{xy}^4) and coupling magnitudes. From the determinant of 2×2 Σ -matrix of beam distribution as given in Eqn. (42), a squared 2-dimensional rms emittance in the horizontal plane can be calculated.

$$\epsilon_{x, rms}^2 = \det \begin{vmatrix} \langle (\Delta x_\beta)^2 \rangle & \langle \Delta x_\beta \Delta \mathcal{P}_x \rangle \\ \langle \Delta \mathcal{P}_x \Delta x_\beta \rangle & \langle (\Delta \mathcal{P}_x)^2 \rangle \end{vmatrix} \quad (45)$$

Likewise, for the counterpart on the vertical plane. For the computation of 4-dimensional rms emittances and couplings, we first define 4-component column matrices ($\mathcal{M}_{4, xy}$, $\mathcal{M}_{4, yz}$, and $\mathcal{M}_{4, xz}$) in two planes as in Eqn. (46). By means of generating 4×4 Σ -matrices with the column matrices as in Eqn. (47), we can calculate the determinant of each

4×4 matrix as described in Eqns. (48) through (49) to follow:

$$\mathcal{M}_{4, xy} = \begin{bmatrix} \Delta x_\beta \\ \Delta \mathcal{P}_x \\ \Delta y_\beta \\ \Delta \mathcal{P}_y \end{bmatrix} \quad \mathcal{M}_{4, xz} = \begin{bmatrix} \Delta x_\beta \\ \Delta \mathcal{P}_x \\ \delta \tilde{E} \\ \Delta \phi \end{bmatrix} \quad \mathcal{M}_{4, yz} = \begin{bmatrix} \Delta y_\beta \\ \Delta \mathcal{P}_y \\ \delta \tilde{E} \\ \Delta \phi \end{bmatrix} \quad (46)$$

$$\begin{cases} \Sigma_{xy} = \Sigma(x_\beta, x'_\beta, y_\beta, y'_\beta) = \langle \mathcal{M}_{xy} \mathcal{M}_{xy}^T \rangle \\ \Sigma_{xz} = \Sigma(x_\beta, x'_\beta, \delta \tilde{E}, \phi) = \langle \mathcal{M}_{xz} \mathcal{M}_{xz}^T \rangle \\ \Sigma_{yz} = \Sigma(y_\beta, y'_\beta, \delta \tilde{E}, \phi) = \langle \mathcal{M}_{yz} \mathcal{M}_{yz}^T \rangle \end{cases} \quad (47)$$

in which \mathcal{M}^T denote a transpose matrix of \mathcal{M} .

$$\epsilon_{xy}^4 = \det \begin{vmatrix} \langle (\Delta x_\beta)^2 \rangle & \langle \Delta x_\beta \Delta \mathcal{P}_x \rangle & \langle \Delta x_\beta \Delta y_\beta \rangle & \langle \Delta x_\beta \Delta \mathcal{P}_y \rangle \\ \langle \Delta \mathcal{P}_x \Delta x_\beta \rangle & \langle (\Delta \mathcal{P}_x)^2 \rangle & \langle \Delta \mathcal{P}_x \Delta y_\beta \rangle & \langle \Delta \mathcal{P}_x \Delta \mathcal{P}_y \rangle \\ \langle \Delta y_\beta \Delta x_\beta \rangle & \langle \Delta y_\beta \Delta \mathcal{P}_x \rangle & \langle (\Delta y_\beta)^2 \rangle & \langle \Delta y_\beta \Delta \mathcal{P}_y \rangle \\ \langle \Delta \mathcal{P}_y \Delta x_\beta \rangle & \langle \Delta \mathcal{P}_y \Delta \mathcal{P}_x \rangle & \langle \Delta \mathcal{P}_y \Delta y_\beta \rangle & \langle (\Delta \mathcal{P}_y)^2 \rangle \end{vmatrix} \quad (48)$$

In the same fashion, we can compute 4-dimensional emittances and couplings in $x-z$ and $y-z$ planes as well.

$$\epsilon_{xz}^4 = \det \begin{vmatrix} \langle (\Delta x_\beta)^2 \rangle & \langle \Delta x_\beta \Delta \mathcal{P}_x \rangle & \langle \Delta x_\beta \delta \tilde{E} \rangle & \langle \Delta x_\beta \Delta \phi \rangle \\ \langle \Delta \mathcal{P}_x \Delta x_\beta \rangle & \langle (\Delta \mathcal{P}_x)^2 \rangle & \langle \Delta \mathcal{P}_x \delta \tilde{E} \rangle & \langle \Delta \mathcal{P}_x \Delta \phi \rangle \\ \langle \delta \tilde{E} \Delta x_\beta \rangle & \langle \delta \tilde{E} \Delta \mathcal{P}_x \rangle & \langle (\delta \tilde{E})^2 \rangle & \langle \delta \tilde{E} \Delta \phi \rangle \\ \langle \Delta \phi \Delta x_\beta \rangle & \langle \Delta \phi \Delta \mathcal{P}_x \rangle & \langle \Delta \phi \delta \tilde{E} \rangle & \langle (\Delta \phi)^2 \rangle \end{vmatrix} \quad (49)$$

$$\epsilon_{yz}^4 = \det \begin{vmatrix} \langle (\Delta y_\beta)^2 \rangle & \langle \Delta y_\beta \Delta \mathcal{P}_y \rangle & \langle \Delta y_\beta \delta \tilde{E} \rangle & \langle \Delta y_\beta \Delta \phi \rangle \\ \langle \Delta \mathcal{P}_y \Delta y_\beta \rangle & \langle (\Delta \mathcal{P}_y)^2 \rangle & \langle \Delta \mathcal{P}_y \delta \tilde{E} \rangle & \langle \Delta \mathcal{P}_y \Delta \phi \rangle \\ \langle \delta \tilde{E} \Delta y_\beta \rangle & \langle \delta \tilde{E} \Delta \mathcal{P}_y \rangle & \langle (\delta \tilde{E})^2 \rangle & \langle \delta \tilde{E} \Delta \phi \rangle \\ \langle \Delta \phi \Delta y_\beta \rangle & \langle \Delta \phi \Delta \mathcal{P}_y \rangle & \langle \Delta \phi \delta \tilde{E} \rangle & \langle (\Delta \phi)^2 \rangle \end{vmatrix} \quad (50)$$

Hence, *coupling magnitudes* between $x-y$, $y-z$, and $x-z$ can be calculated as follows:

$$\left\{ \begin{array}{l} \Delta \epsilon_{xy}^4 \\ = \left| \epsilon_{xy}^4 - \epsilon_x^2 \cdot \epsilon_y^2 \right| \\ = \left| \underbrace{\sum C_{xy}(\langle \Delta x_\beta \Delta y_\beta \rangle, \langle \Delta x_\beta \Delta \mathcal{P}_y \rangle, \langle \Delta y_\beta \Delta \mathcal{P}_x \rangle, \langle \Delta \mathcal{P}_x \Delta \mathcal{P}_y \rangle)}_{23 \text{ terms}} \right| \\ \\ \Delta \epsilon_{yz}^4 \\ = \left| \epsilon_{yz}^4 - \epsilon_y^2 \cdot \epsilon_z^2 \right| \\ = \left| \sum C_{yz}(\langle \Delta y_\beta \delta \tilde{E} \rangle, \langle \Delta y_\beta \Delta \phi \rangle, \langle \delta \tilde{E} \Delta \mathcal{P}_y \rangle, \langle \Delta \mathcal{P}_y \Delta \phi \rangle) \right| \\ \\ \Delta \epsilon_{xz}^4 \\ = \left| \epsilon_{xz}^4 - \epsilon_x^2 \cdot \epsilon_z^2 \right| \\ = \left| \sum C_{xz}(\langle \Delta x_\beta \delta \tilde{E} \rangle, \langle \Delta x_\beta \Delta \phi \rangle, \langle \delta \tilde{E} \Delta \mathcal{P}_x \rangle, \langle \Delta \mathcal{P}_x \Delta \phi \rangle) \right| \end{array} \right. \quad (51)$$

where $C_{xy}(\dots)$ denotes coupling terms as a function of $\langle \Delta x_\beta \Delta y_\beta \rangle$, $\langle \Delta x_\beta \Delta \mathcal{P}_y \rangle$, $\langle \Delta y_\beta \Delta \mathcal{P}_x \rangle$, and $\langle \Delta \mathcal{P}_x \Delta \mathcal{P}_y \rangle$. Hence, $\Delta \epsilon_{xy}^4$ includes all possible combinations of couplings between transverse and longitudinal planes. What is illustrated by

FIG. 24 is the 2nd-order cross moment of transverse positions ($\langle \Delta x_r \Delta y_r \rangle$) to look into the transverse couplings in the same vertical scale. In the absence of space charge and GMPS noise, transverse coupling is not observed. In the presence of space charge, the magnitude of coupling is slightly increased but still marginal. However, with the GMPS noise alone in the absence of space charge, the coupling is more noticeable and some perturbations appear over 1,000 turns. When the GMPS noise is coupled to the full space-charge effects, the coupling is substantially amplified. In FIG. 25, the turn-by-turn calculations of the cross moments are presented in a form of histogram from which we extract statistics. The distributions are slightly dispersed as each instability (either space charge, or GMPS noise) is individually included. When the GMPS noise is applied to macroparticles in the presence of space charge, the RMS value is larger than that of the noise alone by about a factor of two. As derived in Eqn. (51), the cou-

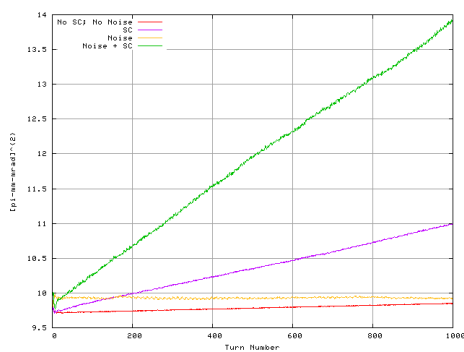


FIG. 26: The time evolution of 4-dimensional coupling, $\Delta\epsilon_{xy}^4$

pling between horizontal and longitudinal planes are continually growing when the GMPS noise and space charge impinge on the Booster beam. In FIG. 26, progressing from bottom to top, each trace line corresponds with each of the following cases: (1) without space charge, nor GMPS noise, (2) GMPS noise alone, (3) space charge alone, (4) GMPS noise in the presence of space charge. In accordance with Eqn. (51), the vertical axis is in units of $(\pi\text{-mm-mrad})^2$. It is evident from the FIG. 26 that transverse coupling is synergistically amplified when the GMPS noise is coupled to full space-charge effects in comparison with the other cases. From the coupling calculations of $\Delta\epsilon_{xy}^4$ and $\langle \Delta x_r \Delta y_r \rangle$, we obtain consistent results that the space charge amplifies the impact of GMPS noise on the Booster beam.

C. Halo Amplitudes

The computation of maximum extent of macroparticle coordinates in a beam at each tracking turn is implemented in the Noise module. The Eqn. (52) includes only physical coordinates (x and y) of a maximum-displaced macroparticle at the location of a random noise node [1]. We refer it to as *halo*

amplitude ($R_{H, 2}$):

$$\mathcal{R}_{H, 2} = \sqrt{x^2 + y^2} \Big|_{Max} \quad (52)$$

In Eqn. (53), *halo amplitude* in 4 dimension, ($R_{H, 4}$), which includes horizontal and vertical positions and angles of a maximum-displaced particle is given:

$$\mathcal{R}_{H, 4} = \sqrt{(x/\sqrt{\beta_x})^2 + (\sqrt{\beta_x} \cdot x')^2 + (y/\sqrt{\beta_y})^2 + (\sqrt{\beta_y} \cdot y')^2} \Big|_{Max}, \quad (53)$$

where β_x and β_y are optics functions at the location of a noise node. Calculations of two types of halo amplitudes ($\mathcal{R}_{H, 2}$ and $\mathcal{R}_{H, 4}$) yield consistent results. FIG. 27 illustrates the evolution of halo amplitudes in green and smoothed data in blue. Due to the large oscillatory behavior of the halo amplitudes, the data is smoothed. The smoothed curve in FIG. 28 shows us with clarity a growing pattern of a maximum-displaced macroparticle from the physical center of a magnet aperture.

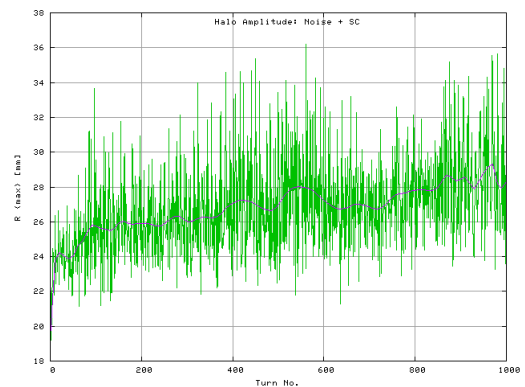


FIG. 27: Halo amplitudes (R_{max}): noise in the presence of the space-charge effects; the blue trace in the background indicates smoothed curve with spline function.

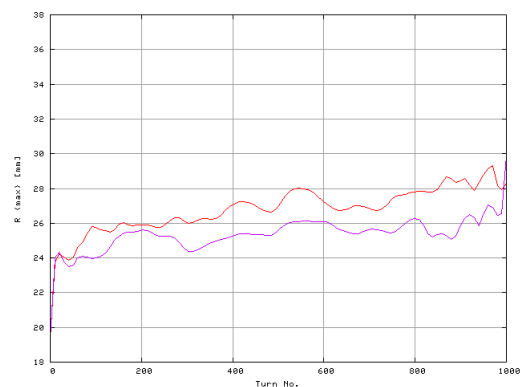


FIG. 28: Halo amplitudes (R_{max}): noise along with space-charge effects (red) vs. space-charge effects alone (blue)

X. CONCLUDING REMARKS

The model presented in this paper is the first-ever measurement-based stochastic noise model for an existing low- γ accelerator lattice structure. Utilizing the parallel computing method, we successfully incorporated a sufficiently large number of macroparticles for better accuracy. The presence of a substantial amount of offending ripple current induced by common-mode voltage in the Booster power system were discovered. On the other hand, it was diagnosed that the differential-mode voltage at each GMPS is well-smoothed with the aid of a 15-Hz low-pass filter installed in each GMPS unit. Moreover, the root causes of the presence of common-mode voltage at each of four GMPS' were diagnosed. The parameterization of the Booster GMPS noise from the ripple-current measurements was achieved by means of extracting time step, autocorrelation time, and noise strength after matching FFT power spectral densities between physical noise and modeled Ornstein-Uhlenbeck noise.

The foregoing results from particle tracking, including power-supply noise as perturbation and space charge as collective effects, make evident that non-white noise originating from power supplies under the influence of space charge leads synergistically to an enhancement of beam degradation phenomena—emittance growth, halo formation, and consequential beam loss—at the injection energy of the Booster.

As was aforementioned, our investigations evidenced that the adverse effects of ripple current are dependent upon the strength of space charge. As a relevant side, we can consider two approaches to coping with the impact that ripple current has on charged-particle beams under the influence of space charge. The first is to reduce inherent space charge forces themselves. Over the past years, the efforts have been made to reduce the space-charge effects in the accelerator system at Fermilab. For instance, in 1993 Fermilab's proton linac was upgraded from a beam kinetic energy of 200 MeV to 400 MeV in order to reduce the space-charge effects in the Booster. Be-

sides, with a proper choice of RF system and RF parameters, space-charge effects can be further reduced in high-intensity proton machines by means of maneuvering charge distribution in longitudinal direction [5]. Accordingly, attendant beam degradation phenomena induced by fluctuating current and space charge can be suppressed. The second approach is to devise instrumental techniques to cancel out common-mode-conducted EMI originating from power supplies.

Upon including more realistic and *non-uniform* charge-density distribution [16], the effects of space charge increases, so does the impact of current fluctuations on the Booster beam accordingly. It is speculated that power-supply ripple current can induce more prominent development of beam degradation process in storage rings of space-charge-dominated regime over long period of time.

Acknowledgments

The author is grateful to University-Fermilab Ph.D. program committee, Prof. A. Bodek, and Dr. W. Chou for their support and supervision during the course of investigations on the impact of current fluctuations and modeling efforts as part of his Ph.D. program. The late Prof. C. L. Bohn of the Northern Illinois University will be remembered for his steadfast encouragement in building the stochastic noise model. The author also wish to thank Fermilab staff members of Accelerator Division for helpful discussions and useful provisions, and of Computing Division for their arrangement made to use local workstation clusters. Special thanks should go to Accelerator Physics Group of SNS/ORNL for their support in commissioning and upgrading the ORBIT-FNAL at the outset of the efforts.

This work was supported by Fermi Research Alliances (FRA), LLC., under the U.S. Department of Energy (DOE) contract No. DE-AC02-76-CH03000, and by DOE Grant No. DE-FG02-91ER40685 to University of Rochester.

-
- [1] C. L. Bohn, *Collective Modes and Colored Noise as Beam Halo Amplifiers*, AIP Conf. Proc., **737**, 2004, pp. 456—461
 - [2] J. Galambos, *ORBIT—A Ring Injection Code With Space Charge*, Proceedings of PAC, New York, 1999
 - [3] G. E. Uhlenbeck and L. S. Ornstein, Phys. Rev., **34**, 823, 1930, pp. 823—841
 - [4] N. G. Van Kampen, *Stochastic Processes in Physics and Chemistry*, (North-Holland, 1992), pp. 39, 53, 59, 60, 73, 225, 232
 - [5] P. S. Yoon, D. E. Johnson, and W. Chou *The Modeling of Microbunch Injection into the Main Injector* Fermilab-TM-2368-AD-APC
 - [6] N. Mohan, T. Undeland, and R. Robbins, *Power Electronics*, John Wiley & Sons, pp. 500—501, 1989
 - [7] P. Horowitz and W. Hill, *The Art of Electronics*, Cambridge University Press, 1989
 - [8] A. Einstein and L. Hopf, Ann. d. Phys., **33**, 1105, 1910
 - [9] A. Einstein, R. H. Fürth Ed. *Investigations on the Theory of Brownian Movement*, Methuen, London, 1926, Dover Publication, New York, 1956
 - [10] P. Langevin, *Sur la Théorie du motion de brownien*, Comptes Rendus Acad. Sci. (Paris), **146**, 1908, pp. 530—533
 - [11] G. I. Taylor, *Proc. London Math. Soc.* **22**, 196 (1920)
 - [12] J. L. Doob, *The Brownian Movement and Stochastic Equation*, Annals of Mathematics, **43**, 2, 1942, pp. 351—369
 - [13] M. G. Wang and G. E. Uhlenbeck, *On the Theory of the Brownian Motion II*, Rev. Mod. Phys. **17**, 2—3, 1945, pp. 323—342
 - [14] G. E. P. Box and M. E. Muller, *A Note on the Generation of Random Normal Deviates*, Annals Math. Stat., **29**, 2, 1958, pp. 610—611
 - [15] W. H. Press, B. P. Flannery, S. A. Teukolsky, *Numerical Recipes in C++*, (Cambridge University, Cambridge, 1998), pp. 292—293
 - [16] P. S. Yoon, Chapters 2—4, and 7, Ph.D. dissertation, *Error-Induced Beam Degradation in Fermilab's Accelerators*, 2007, Fermilab-thesis-2007-43
 - [17] J. Engelbert, T. Nguyen and C. Thurston, *B2 Spice A/D Version 4 User's Manual*, Beige Bag Software, Inc., 2002
 - [18] MAD 8 home page: <http://hansg.home.cern.ch/hansg/>

[mad/mad8/mad8.html](#)

- [19] M. Reiser, *Theory of Charged Particle Beams*, Wiley & Sons, 1994
- [20] R. L. Stratonovich, *Introduction to the Theory of Random Noise, Vol. I and II*, Gordon and Breach, New York, 1963